Double Perovskite Solar Cells

Submitted by

Saikat Samadder

Roll no : 308043

Registration no : VB-868 2021-22

Under the supervision of

Dr. Swapan K. Mandal

For the fulfilment of M.Sc. semester 4 dissertation paper

Department of Physics

Visva-Bharati, Santiniketan

May 2023

Certificate from Supervisor

This is to certify that the dissertation work entitled "Double Perovskite" has been undertaken and written under my supervision and it describes the original work carried out by Saikat Samadder for the partial fulfilment of M.Sc. degree.

Date: _____

_____

Dr. Swapan K. Mandal

Department of Physics

Siksha-Bhavana

Visva-Bharati, Santiniketan

Contents

Abstract

Meeting the enormous energy demand of our modern world solely through fossil fuels is a daunting challenge. As a result, researchers are investigating smart and useful materials that can transform light into usable energy as a renewable energy source. Perovskite solar cells (PSC) are considered a game-changer in the field of photovoltaics due to their enormous advancement in power conversion efficiency (PCE), increasing from 3.8% to 25% in just a few years. In this study, we provide a brief introduction to the charge generation and charge transport in perovskite solar cells and the underlying physics. We use the Solar Cell Capacitance Simulator (SCAPS-1D) application to simulate the physical properties of the solar cell, and we discuss the numerical methods related to this. We employ an inorganic double perovskite Cs_2BiAgI_6 material as an active layer for solar cell fabrication and investigate the device configuration ITO/TiO_2/Cs_2BiAgI_6/CBTS/Au. We vary the solar cell active layer thickness, bandgap, doping concentration, and temperature to study the device's performance. We also investigate the effect of donor concentrations by changing its value for the proposed device from 1×10^{-12} cm^{-3} to 1×10^{-20} cm^{-3}. The power conversion efficiency of the perovskite solar cell is improved by using several charge transport materials. Our simulation analysis demonstrates that the suggested design could be used to create a device for enhancing the effectiveness of the perovskite solar cell.

Introduction

World's energy demand is increasing significantly because of population growth and industrial evolution. It is important to note that the population has increased by 2 billion just in one generation and major contribution has been given by developing countries. Preventing an energy crisis in one of the most casual issues of the 21st century. Energy demand is therefore increasing fast as to meet the requirements of growing population in the world. Different countries in the world have their own strategies, plans, policies and control measures to establish themselves in the world. As of the population growth and development initiatives, resources available in the world are getting depleted [1]. Considering energy sources is therefore very important as they play a key role in satisfying the need of the world and living population. Accessible energy is not sufficient to people, because of several reasons such as developmental profile of a country, economic status of people and nature of technological advancements of the country. Ecosystem is polluted heavily because of the emission of various gases generated from burning of fossil fuel which are readily available and commonly used for satisfying energy demand of the world [2]. Developing countries are now put into pressure to search for the sources of energy as their population growth is high and they are seeking for economic development to become economically viable [3]. As economic development takes place, energy demand also increases since it is proportional to economic growth. Introducing non renewable energy sources would not definitely meet energy demand since they are exhaustible and limited source of energy [4]. Many countries relay on exhaustible energy sources than renewable energy sources. Continuous use of non-renewable energy sources may lead to climate change, soil degradation, destruction of the ozone layer, global warming, air pollution, acid rain, etc. which may in turn end up with heavy natural disasters damaging ecosystems of the planet [5]. It is therefore vital to go for eco-friendly energy sources for the betterment of the future world [6]. Considering renewable energy sources such as solar energy, wind energy, hydropower and geothermal, is critically important in this sense as they are eco-friendly [7].

However, solar energy could be a best option for the future world because of several reasons: First, solar energy is the most abundant energy source of renewable energy and sun emits it at the rate of 3.8 - 1023 kW, out of which approximately 1.8 - 1014 kW is intercepted by the earth[8]. Solar energy reaches the earth in various forms like heat and light. As this energy travels, majority of its portion is lost by scattering, reflection and absorption by clouds.

Studies revealed that global energy demand can be fulfilled by using solar energy satisfactorily as it is abundant in nature and freely available source of energy with no cost [9]. Second, it is a promising source of energy in the world because it is not exhaustible, giving solid and increasing output efficiencies than other sources of energy [5].

Photovoltaic (PV) technology is used to convert sunlight into electricity directly without any interface for conversion. Solar radiation distribution and its intensity are two key factors which determine efficiency of solar PV industry. Such two parameters are highly variable over the countries. It has clearly been indicated in Fig. 1. Asian countries have highest potential to receive solar radiation compared to other temperate countries as sunshine duration in such countries is high in a year
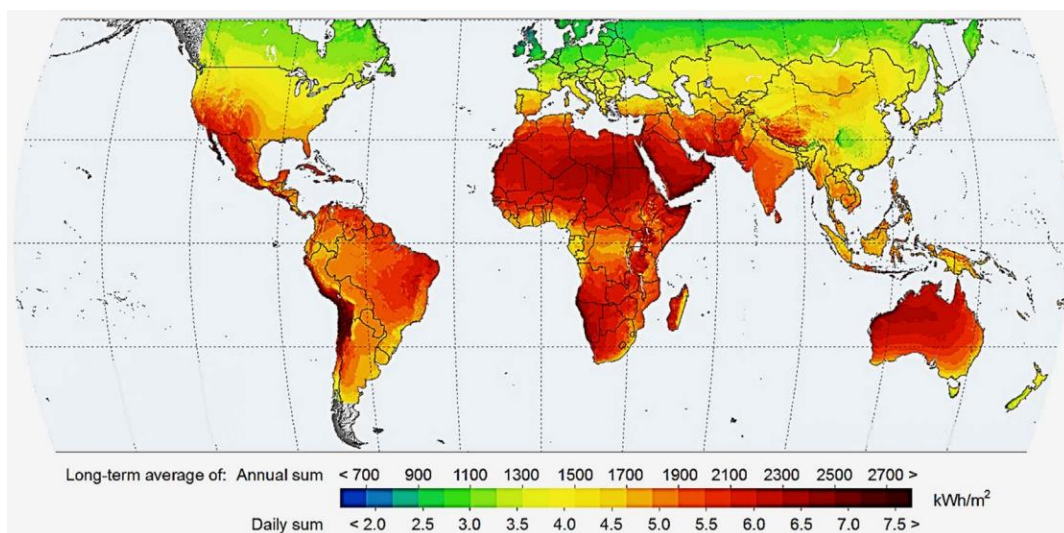
Figure 1 Maps of global horizontal irradiation (GHI)

Photovoltaic technology

The major benefit of solar energy over other conventional power generators is that the sunlight can be directly converted into solar energy with the use of smallest photovoltaic (PV) solar cells. In other words, we say that this is a technology used to convert sunlight into electricity directly without any interface for conversion. There has been a large amount of research activities to combine the Sun's energy process by developing solar cells/panels/module with high converting form. The most advantages of solar energy are that it is free reachable to common people and available in large quantities of supply compared to

that of the price of various fossil fuels. Solar energy requires considerably lower manpower expenses over conventional energy production technology.

Types of PV cells

Solar cells are typically named after the semiconducting material they are made of. These materials must have certain characteristics in order to absorb sunlight. Some cells are designed to handle sunlight that reaches the Earth's surface, while others are optimized for use in space. Solar cells can be made of only one single layer of light-absorbing material (single-junction) or use multiple physical configurations (multi-junctions) to take advantage of various absorption and charge separation mechanisms.

Solar cells can be classified into first, second and third generation cells. The first-generation cells also called conventional, traditional or wafer-based cells are made of crystalline silicon, the commercially predominant PV technology, that includes materials such as polysilicon and monocrystalline silicon. Second generation cells are thin film solar cells that include amorphous silicon, CdTe and CIGS cells and are commercially significant in utility-scale photovoltaic power stations, building integrated photovoltaics or in small standalone power system. The third generation and fourth generation of solar cells includes a number of thin-film .Many use organic materials, often organometallic compounds as well as inorganic substances. [10]
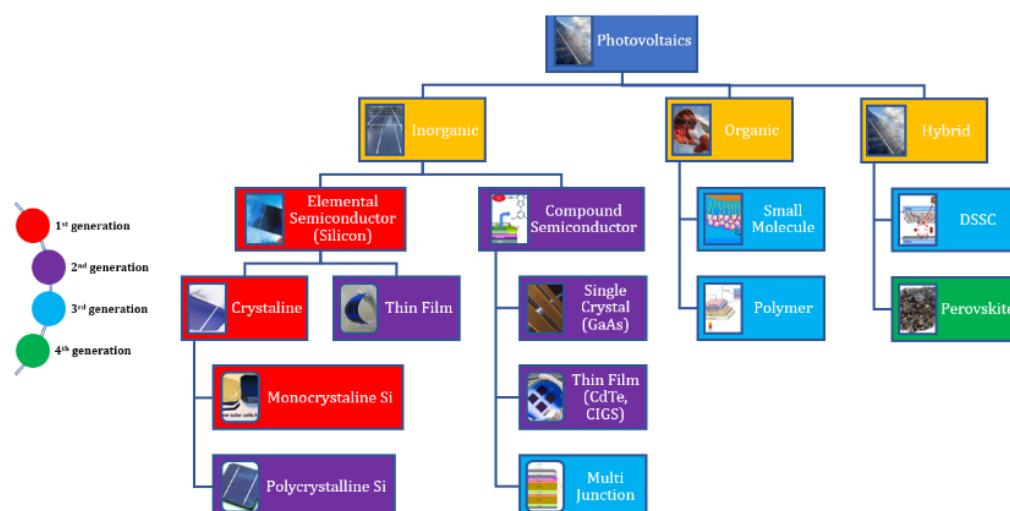

Figure 2 Types of solar cell

Perovskite solar cell

In 1839, Edmund Becquerel was the first to convert sunlight into electricity. In 1873, Willoughby Smith discovered photoconductivity (PC) in selenium. In 1883, Charles Fritts proposed the first design of PV cell, which was based on the Selenium wafers. The theory of photo-electric effect proposed by Albert Einstein in 1905 explained how light knocks out the electron from the metal surface. Later for this work, he was awarded with the Nobel Prize. In 1918, Jan Czochralski laid the foundation of Silicon (Si) based solar cells by developing a technique to grow single-crystal silicon (Si). In 1954, the birth of PV occurred, when the crystalline silicon-based solar cell was developed in Bell lab, USA that had power conversion efficiency (PCE) of 4.5%. Since then, researchers have been actively searching for a low-cost device structure and some new materials exhibiting the PV effect. As a result, second-generation solar cells came into existence. These cells were basically based upon III-V device existence. These, and CIGs solar cells were introduced in the field of solar photovoltaics. The early 1990s came up with the third generation of solar cells with Dye-sensitized structure. In 2000s Organic Photovoltaic cells (OPV) were introduced. Currently, crystalline silicon solar cells dominate the market, but the factors, such as the requirement of the expensive manufacturing process and costly raw materials are urging researchers to come up with a new PV technology that has the combination of both high efficiency and low-cost manufacturing.[11]

Perovskite material

The perovskite materials are gaining huge interest among the researchers because of their brilliant PV performance, low-cost raw material, and requirement of easy processing conditions. The PSCs do not require any sophisticated processing conditions; instead, they can be synthesized in laboratories using wet chemistry with the help of simple low-cost techniques, such as spin coating, dip coating, screen printing, dual source evaporation techniques, etc. The perovskite materials can also be grown on a flexible substrate. Despite all the merits, poor device stability and short lifetime are creating hindrances in the path of commercialization of PSCs. The enormous capability of PSCs is evident from the abrupt increment in the power conversion efficiency (PCE) from 3% to 25.2% (28% in tandem architecture) over the past 10 years. While other technologies took nearly 30 years to witness this milestone. Perovskites material incorporated in a solar cell can serve as both, an absorber

layer and an efficient charge transport layer. The performance comparison of PSC and Silicon solar cell is illustrated in Figure 3.
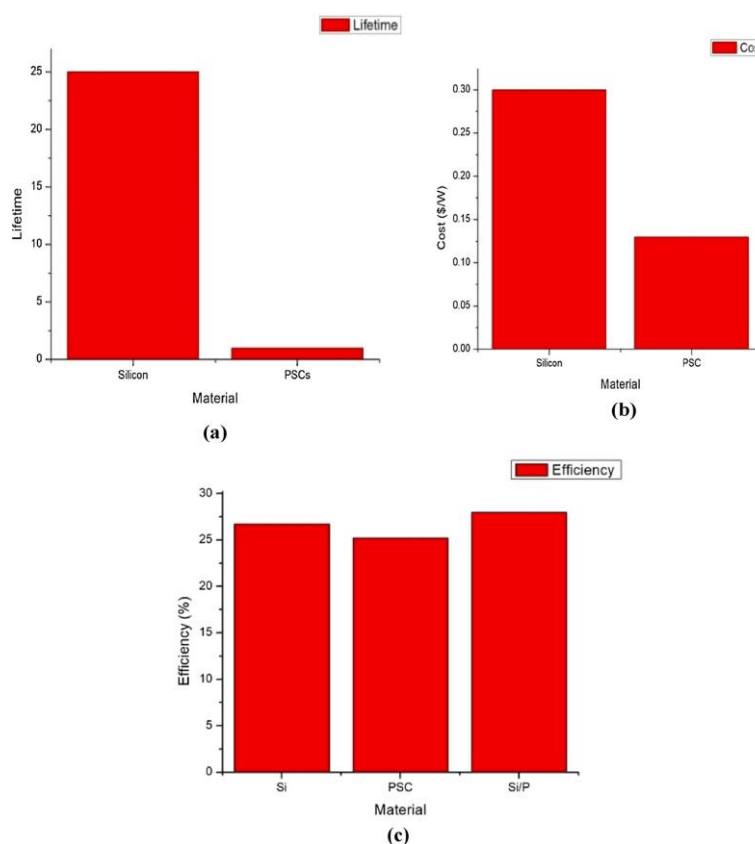
Figure 3. Comparison of performance of PSC and Silicon solar cell (a) comparison of cost (b) comparison of lifetime (c) comparison of efficiency of silicon, PSC and Si/P tandem cell.

Perovskite material properties

The perovskite materials are considered as one of the eminent materials for new generation PV technology because of their unique properties, such as high electron mobility (800 cm2/Vs), high carrier diffusion length (exceeding 1 µm), an bipolar charge transport behavior, high absorption coefficient (greater than 105 cm−1) due to s-p antibonding coupling, low exciton binding energy (less than 10 m eV), high photo luminesce (PL) quantum efficiency (as high as 70%), high carrier lifetime (exceeding 300 ns), optimum bandgap, low surface recombination velocity, tunable bandgap, great structural defect tolerance, and amiable grain boundary effect. The main difference between inorganic and organic absorbers is in the exciton type. The organic absorber layer has basically Frenkel type exciton while the inorganic layer has Wannier type. The perovskite material used in solar cells has Wannier

type exciton. Therefore, the generated charge carriers behave in the same manner as they do in inorganic material. The properties of perovskite materials are summarized in the Table 1 and the PCE of various cells to date is shown in Table 2. The properties indeed are adjustable by controlling the shape and size of the constituent particles during fabrication.

Table 1 Properties of perovskite materials

Properties	Value Range
Bandgap	1.5–2.5 eV
Absorption coefficient	105 cm−1
Exciton binding energy	Less than 10 m eV
Crystallization energy barrier	56.6–97.3 kJ mol−1
PL quantum efficiency	70%
Charge carrier lifetime	Greater than 300 nm
Relative permittivity	3
Carrier mobility	800 cm /Vs
Trap-state density	1010 cm3 (single crystals), 1015–1017 cm3 (polycrystal

Table 2 The PCE of various PV cells to date

Solar cell	Types	Efficiency[12]	Developer name
Silicon	Single crystal	26.1	ISFH (Institute for Solar Energy Research Hamelin)
	Poly-cry	22.3	FhG-ISE (Fraunhofer Institute for Solar Energy Systems)
	Thin film	21.2	Solexel
	a-Si:H	14	AIST (National Institute of Advanced Industrial Science and Technology)
	Silicon hetero structure	26.7	Kaneka (Kaneka Solar Energy)
GaAs	Single crystal	27.8	LG (LG Electronics)
	Thin-film	29.1	Alta device
CIGS		23.4	SolarFron (Solar Frontier)
CdTe		22.1	FirstSolar (First Solar Inc)
Quantum dot		16.6	Univ. Of Queensland
Dye-sensitized		11.9	Sharp (Sharp Solar)
Organic		16.5	SCUT-CSU (South China University of Technology - Central South University)

Perovskite	25.2	KRICT/MIT (Korea Research Institute of Chemical Technology/ Massachusetts Institute of Technology)

Historical background of PSCs

The perovskite is basically Calcium titanium oxide ($CaTiO_3$). It is a mineral found by Gustav Rose in the Ural Mountains of Russia in 1939. Count Lev Alekseevich Perovski (1972–1856), a Russian mineralogist further carried the research and thus, the material was named after him as 'Perovskite' [13]. In the 1990 s, Mitzi and co-workers investigated the optoelectronic properties of the organic–inorganic perovskites. They reported that the material exhibited strong exciton features, and further suggested that it could be used in the field of LEDs, transistors and solar cells [14]. The phenomenon of PV generation was first seen in this material by Kojima and coworkers. In 2009, they were first to use perovskite material in solar cells by utilizing it as a liquid sensitizer in DSSC configuration. The $MAPbI_3$ and $MAPbBr_3$ (where MA stands for CH_3NH_3) were used as liquid sensitizers, and the device attained an efficiency of 3.81% and 3.2%, respectively. However, the device was highly unstable and lasted only for a few seconds due to the presence of liquid electrolyte [15]. Park et al. used quantum dots of nanocrystalline material and utilized similar dye-sensitized concepts. They raised the cell efficiency from 3.8% to 6.54%, but the device collapsed after 10 min of successful operation due to the dissolution of MAPbI3 quantum dots into the redox electrolyte solution [16]. Because of the instability raised due to the presence of liquid electrolytes, this configuration did not gain much attention. In 2012, Kim et al. overcame the problem arising due to the presence of liquid electrolytes by fabricating an all-solid-state PSC. The Spiro-OMeTAD was used as a hole transport layer and the device attained an efficiency of 9.7%. This made a remarkable change in the history of the perovskite sensitized solar cells as it not only raised the efficiency but also made a considerable enhancement in the lifetime by withstanding exsitu long term stability test for about 500 h without any encapsulation [17].In 2013, Burschka et al. obtained an efficiency of 15% by using the 2-step sequential deposition technique, and fabricated the cell in planar architecture. They adopted the sequential deposition technique where they first deposited PbI_2 layer followed by deposition of CH_3NH_3I in- stead of processing both of them together. This structure gave a high J_{sc} (20

mA/cm2) due to the creation of a dense and uniform perovskite layer [18]. In 2014, Im et al, fabricated MAPbI$_3$ based solar cells using two-step solution processing. They attained a high performance by controlling the size of MAPbI$_3$ cuboid, which enabled proper light-harvesting and enhanced charge transportation. They re- ported that the cuboid size depended on the concentration of MAI solution and also upon the exposure time of PbI$_2$ to MAI before spin coating. This group of researchers obtained an improved PSC with an efficiency of 17.01% [19]. Giordano et al. in 2015, improved the electronic properties of mesoporous Titania layer (m-TiO$_2$) by the addition of Lithium (Li) in it and attained superior device performance with PCE of 19.3%. The Li doped mesoporous Titania layer (m-TiO$_2$) gave better electronic properties and faster electronic trans- portation due to the reduction in electronic trap states. This device exhibited negligible hysteresis loss (less than 0.3%) [20]. In 2015, Yang et al. demonstrated a technique to deposit improved quality FAPbI3 film with (1 1 1) crystallographic orientation, uniform, dense and large microstructures. They used FAPbI3 instead of MAPbI3 and attained power conversion efficiency (PCE) of 20.2% [21].In 2016, Li et al. fabricated a perovskite film with uniform morphology and crystalline behavior by using the vacuum flash solution processing method (VASP). They used FA0.81MA0.15PbI2.51Br0.45 as an absorber layer and attained PCE of 20.5% [22]. In 2016, Bi et al. introduced a new approach for perovskite film fabrication and attained improved electronic property by using a polymer. They improved the growth and nucleation processes by using poly (methyl methacrylate) (PMMA) and attained PCE of 21.6% [23]. Recently, Yang et al. used multiple cations (comprising FA) and mixed halide anion as an absorber layer. They succeeded in reducing the concentration of deep-level defect states by the addition of iodide solution into the organic cation solution. This defect engineering enabled the scientists to achieve an efficiency of 22.1% for small scale and 19.7% in 1 cm2 cell [24].Then came the breakthrough in 2018 when researchers from Chinese Academy of Sciences attained the highest efficiency of 23.3%. Further, in December last year, the maximum efficiency of single-junction silicon solar cell was defeated by Perovskite in tandem architecture along with Silicon by attaining PCE of 28%. The efficiency of single-junction PSC was raised to 23.7% and high Voc closer to the bandgap was attained by tailoring a high quality perovskite layer offering minimum recombination loss [25]. Currently, the highest efficiency of single-junction PSC has reached 25.2% by KRICT (South Korea). They used a highly efficient hole conductor layer, Nickel oxide (Nix), which is deposited over a large area. NiO$_x$ is an inexpensive material and it has ability to withstand high temperatures up to 70 °C. The layers were deposited by rotatory coating method [26]. The advancement in the progress of PSCs in
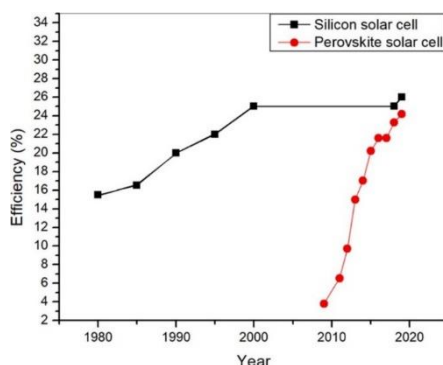
past years is shown in Fig. 2.

Figure 4 Recorded Power Conversion Efficiency of the PSC in progressive years.

It is seen that, as compared to silicon solar cells the PSCs exhibit rapid development. The details of PSCs are enclosed in Table 3. It is important to note that all the leading perovskite solar cells (PSCs) have the incorporation of Formamidinium (FA) as cation which is also believed to be more stable than Methylammonium (MA) and also has an optimal red-shifted bandgap. However, the size of FA is very large, which produces lattice distortion [27].Now the power conversion efficiency (PCE) of perovskite-based solar cells is expected to reach up to 30% by 2020. Apart from the extensive research going in efficiency hike, work is also being done to increase the stability and lifetime of perovskite solar cells (PSC). Gracini et al. engineered an ultra-stable 3D/2D CH3NH3PbI3 perovskite junction that had PCE of 13% and was stable for one year [28]. Hwang et al. used a layer of Polytetrafluoroethylene, a hydrophobic polymer over the top of the PSC and noticed a minimal degradation for over 30-days in ambient air condition [19]. From all these works, it is concluded that it is one of the most rapidly growing PV cells with advancements taking place to date.

Table 3 Increment in efficiency in a progressive year

PCE (%)	$V_{oc}(v)$	J_{sc}	FF	Device configuration	Year
3.8	0.61	11	0.57	Pt-FTO/Electrolyte solution/CH3NH3PbI3/TiO2	2009
6.54	0.706	15.82	0.586	Pt/Liquid Electrolyte/CH3NH3PbI3 (QD) / TiO2/FTO	2011
9.7	0.888	17	0.62	Au/spiroOMeTAD/CH3NH3PbI3/mTiO2/FTO	2012
15	0.993	20	0.73	Au/spiroMeOTAD/TiO2/CH3NH3PbI3/Glass	2013
17.01	1.056	21.64	0.741	Au/spiro-MeOTAD/Cuboid MAPbI3/ MAPbI3/m-TiO2/c-TiO2/FTO	2014
19.3	1.114	23	.74	Au/Spiro-OMeTAD/Perovskite/m-LiTiO$_2$/ Perovskite/ FTO	2014
20.2	1.06	24.7	0.775	Au/PTAA/Perovskite/(bl/m-TiO$_2$)/FTO	2015

20.5	1.1143	23.24	0.759	Au/Spiro-OMeTAD/Perovskite/m-TiO₂/ bl-TiO₂/ FTO	2016
21.6	1.14	23.7	.78	Au/Spiro-OMeTAD/Perovskite/m-iO₂/ Perovskite/bl-TiO₂/ FTO	2016
22.1	1.11	25	0.817	FTO/TiO2/m TiO2/perovskite composite layer/perovskite upper layer/PTAA/Au	2018
22.7	1.14	24.92	0.792	FTO/d-TiO2/mp-TiO2/NBH/P3HT/Au	2019

Structural properties of hybrid organic-inorganic perovskite materials

The Perovskite materials comprise the crystal structure similar to Calcium Titanate (CaTiO3) and it follows the general formula of ABX_3 (where X is generally Oxygen, Nitrogen, Carbon or Halogen). Halide perovskites are of two types (i) Alkali halide-based perovskite (ii) Organic-inorganic halide-based perovskite. The Alkali halide-based perovskite comprises of monovalent alkali cation (A) as Cs^+, Rb^+, K^+, Na^+ and Li^+, divalent cation (B) as (Pb^{2+}, Sn^{2+}, Ge^{2+}) and halogen anions (X) as Cl^-, Br^-, I^-, F^-. Organic-inorganic halide based perovskite has organic monovalent cation (A) as $CH_3NH_3^+$, $CH_3CH_2NH_3^+$, $NH_2CHNH_2^+$ [29]. Where 'A' ion having coordinate (0.0, 0.0, 0.0) in the crystal coordinate system and 'B' having coordinate (0.5, 0.5, 0.5) both represent cationic radii, with the size of A usually greater than B, and 'X' represents anionic site with coordinate (0.5, 0.5, 0) The cations 'A' and 'B' coordinates with 12 and 6 'X' anions creating cuboctahedra and octahedral geometries respectively. This halide based perovskite has attractive electrical, optical and magnetic properties that enable users to apply them in the field of solar cells [30]. Ideal perovskite structure has the highest symmetry possessing cubic structure as shown in, Figure the BX_6 octahedral network occupies the corner

12

of the structure while A occupies the interstices. This BX_6 octahedral network plays a vital role in the determination of phase transition, bandgap and transport properties. The perovskite formation tendency can be depicted by using Goldschmidt tolerance factor (t) which is given by

$$t = \frac{R_A + R_B}{\sqrt{2(R_B + R_X)}} \tag{1}$$

$$\mu = \frac{R_B}{R_X} \tag{2}$$

Where R_A, R_B, and R_x represent ionic radii of A, B cation and X anion respectively. The value of the tolerance factor lies between 0.88 and 1.1 for a stable crystal structure of perovskite. It is usually expected that perovskite is stable if 't' lies within the specified range, but it is also seen that perovskite is not stable even if 't' is in the range of 0.8–0.9 [31] . An additional consideration for perovskite formation is taken into account, with the octahedral factor (μ), which is given by Eq. (2). It is used to determine the distortion and stability of the perovskite structure. The perovskite is stabilized for an octahedral factor ranging from 0.45 to 0.89 [32]. The most common absorber material used for PSC is methylammonium lead trihalide (MAPbI$_3$ where X is the halide which can be Cl, Br or I). The unit cell parameters increase from 5.68 to 5.92 to 6.27Â as the size of the halide atom increase from Cl to Br to I. However, the aspherical shape and larger size of Methylammonium (MA) leads to the distortion in the network leading to phase transition with a decrease in the temperature, For T < 160 K, the orthorhombic structure, for 162.2 K < T < 327.4 K tetragonal structure, and for T > 327.4 K cubic structure is observed. The bandgap of methylammonium lead halide usually lies within the range of 1.5–2.3 eV, where MAPbI$_3$ is a direct bandgap material with a bandgap of 1.55 eV approximately, whereas MAPbBr$_3$ has a comparatively wider bandgap of 2.3 eV for 800 nm absorption onset. FAPbI$_3$ (where FA is Formamidinium) shows comparatively narrower bandgap of 1.48 eV, signifying larger current extraction when employed as the absorber layer, but this material has shown lower stability. The structural properties of methylammonium lead halide also show variation depending upon the type of halogen atom used. On using smaller sized Br$^-$ instead of I$^-$ reduces the lattice constant thereby transiting into a more stable cubic phase. This fact is also evident by examining the crystal structure of MAPbI$_3$ and MAPbBr$_3$ which crystallize in the tetragonal form and cubic form respectively.
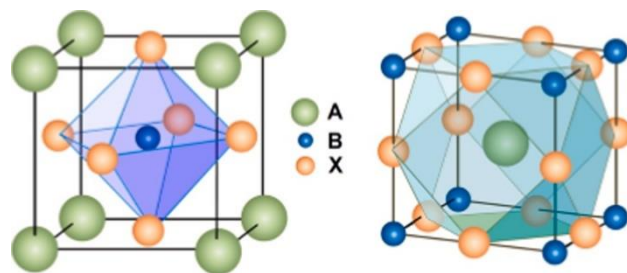
Figure 5 : ABX$_3$ perovskite structure showing (left) BX$_6$ octahedral and (right) AX$_{12}$ cuboctahedra geometry.

Solar Cell Physics

Solar cells and photodetectors are devices that convert an optical input into current. A solar cell is an example of a photovoltaic device, i.e., a device that generates voltage when exposed to light. The photovoltaic effect was discovered by Alexander-Edmond Becquerel in 1839, in a junction formed between an electrode (platinum) and an electrolyte (silver chloride). The first photovoltaic device was built, using a Si pn junction, by Russell Ohl in 1939. The functioning of a solar cell is similar to the photodiode (photodetector). It is a photodiode that is unbiased and connected to a load (impedance). There are three qualitative differences between a solar cell and photodetector

1. A photodiode works on a narrow range of wavelength while solar cells need to work over a broad spectral range (solar spectrum).
2. Solar cells are typically wide area devices to maximize exposure.
3. In photodiodes the metric is quantum efficiency, which defines the signal to noise ratio, while for solar cells, it is the power conversion efficiency, and which is the power delivered per incident solar energy. Usually, solar cells and the external load they are connected to are designed to maximize the delivered power.
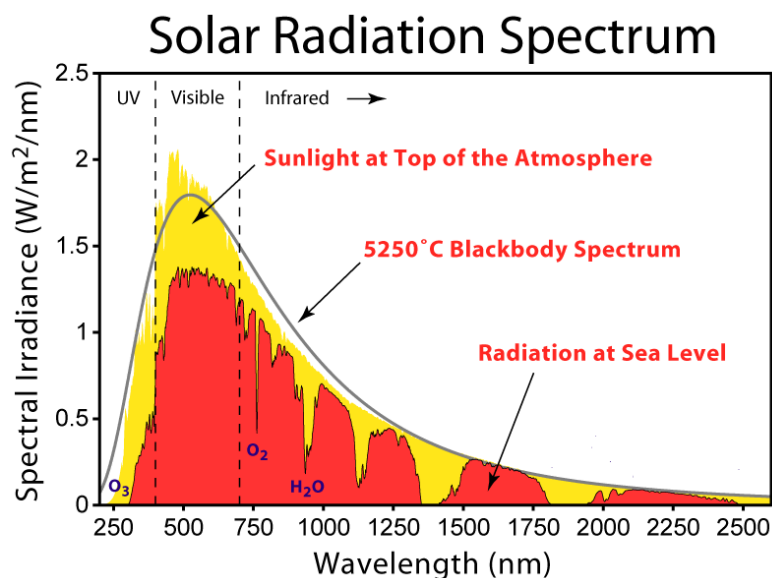

Figure 6 : Typical solar spectrum at the top of the atmosphere and at sea level. The difference is the radiation absorbed/scattered by the atmosphere. The spectrum of a black body at 5250°C is also superimposed and used for modelling. Modified from http://en.wikipedia.org/wiki/Sunlight

Solar Spectrum

The solar spectrum typically extends from the IR to the UV region, wavelength range from 3 μm to 0.2μm. But the intensity is not uniform. A typical solar spectrum, as a plot of spectral irradiance vs. wavelength, is shown in Figure 6.The area under the curve gives the total areal intensity and this is approximately 1.35 kW m-2. The solar spectrum can be approximated by a black body radiation curve at temperature of approximately 5250°C. There is also a difference in the spectra measured at the top of the atmosphere and at the surface, due to atmospheric scattering and absorption. The path length of the light in the atmosphere depends on the angle, which will vary with the time of day. This is given by the air mass number (AM), which is the secant of the angle between the sun and the zenith (sec θ). AM0 represents the solar spectrum outside the earth's atmosphere. AM1 is when the angle is zero, i.e. Sun is at the zenith and it has an intensity of 0.925 kW m^{-2}. AM2 is when sun is at angle of 60° and its intensity is 0.691 kW m-2. The different spectra are plotted in Figure 7.
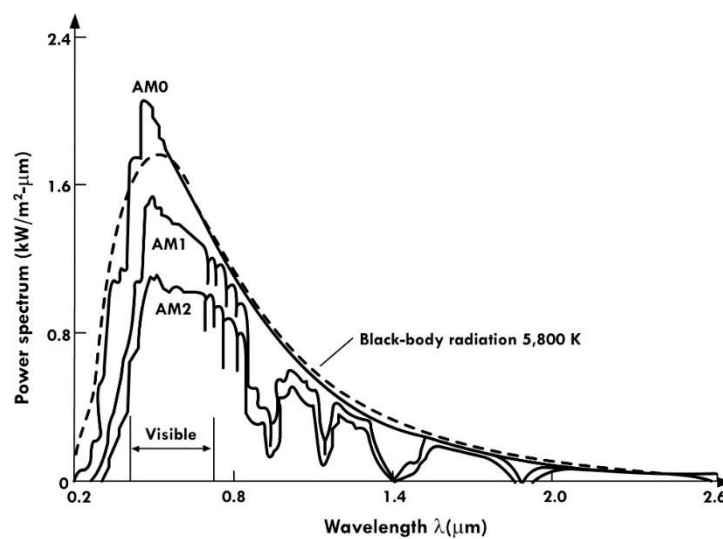

Figure 7. Typical solar spectrum for different air mass conditions. The plot shows AM0 (spectrum outside the atmosphere), AM1 (at the zenith), and AM2 (at an angle of 60˚). This again can be modelled by black body spectrum, at various temperatures. Adapted from Physics of semiconductor devices - S.M. Sze.

The data can also be plotted as a photon flux density i.e., number of photons per unit energy per unit area per unit time. This is shown in Figure 8.

Solar cell working principle

A simple solar cell is a pn junction diode. The schematic of the device is shown in Figure 9. The n region is heavily doped and thin so that the light can penetrate through it easily. The p region is lightly doped so that most of the depletion region lies in the p side. The penetration depends on the wave- length and the absorption coefficient increases as the wavelength decreases. Electron hole pairs (EHPs) are mainly created in the depletion region and due to the built-in potential and electric field, electrons move to the n region and the holes to the p region. When an external load is applied, the excess electrons travel through the load to recombine with the excess holes. Electrons and holes are also generated with the p and n regions, as seen from Figure 9. The shorter wavelengths (higher absorption coefficient) are absorbed in the n region and the longer wavelengths are absorbed in the bulk of the p region. Some of the EHPs generated in these regions can also contribute to the current. Typically, these are EHPs that are generated within the minority
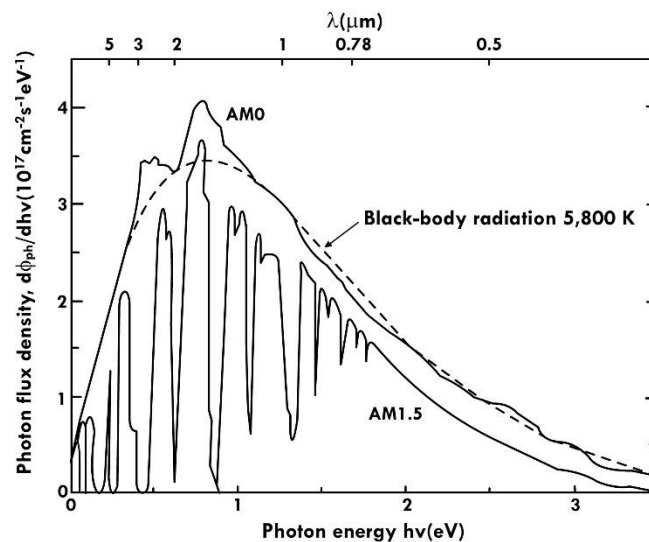

Figure 8 : Solar spectrum plotted as photon flux density vs. energy for AM0 and AM1.5. The difference in the spectra is due to the absorption/scattering by the atmosphere. Adapted from Physics of semiconductor devices - S.M. Sze.

Carrier diffusion length, L_e for electrons in the p side and L_H for holes in the n side. Carriers produced in this region can also diffuse into the depletion region and contribute to the current. Thus, the total width of the region that contributes to the solar cell current is $w_d+L_e+L_h$, where w_d is the depletion width. This is shown in Figure 10. The carriers are extracted by metal electrodes on either side. A finger electrode is used on the top to make the electrical contact,

so that there is sufficient surface for the light to penetrate. The arrangement of the top electrode is shown in Figure 11

Consider a solar cell made of Si. The band gap, E_g, is 1.1 eV so that wavelength above 1.1 µm is not absorbed since the energy is lower than the band gap. Thus, any λ greater than 1.1 µm has negligible absorption. For λ much smaller than 1.1 µm the absorption coefficient is very high and the EHPs are generated near the surface and can get trapped near the surface defects. So, there is an optimum range of wavelengths where EHPs can contribute to photocurrent, shown in Figure 10
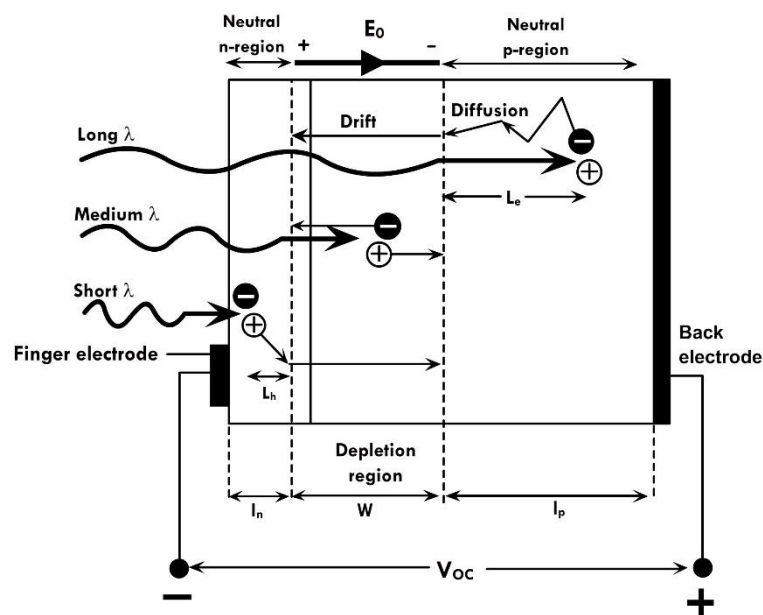

Figure 9 : Principle of operation of a pn junction solar cell. Radiation is absorbed in the depletion region and produces electrons and holes. These are separated by the built-in potential. Depending on the wavelength and the thickness different parts of the device can absorb different regions of the solar spectrum. Adapted from Principles of Electronic Materials - S.O. Kasap
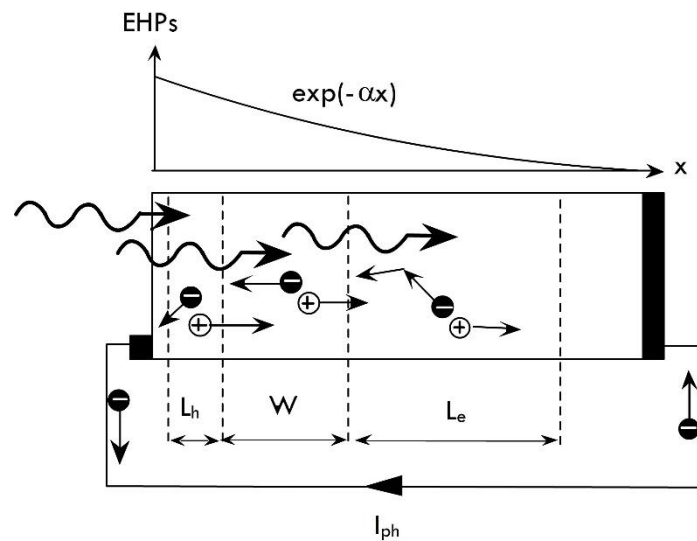
Figure 10 : Photogenerated carriers in a solar cell due to absorption of light. w is the width of the depletion region, while L_h and L_e are minority carrier diffusion lengths in the n and p regions. The amount of absorption reduces with depth and hence the depletion region must be close to the surface to maximize absorption. This is achieved by having a thin n region. Adapted from Principles of Electronic Materials - S.O. Kasap
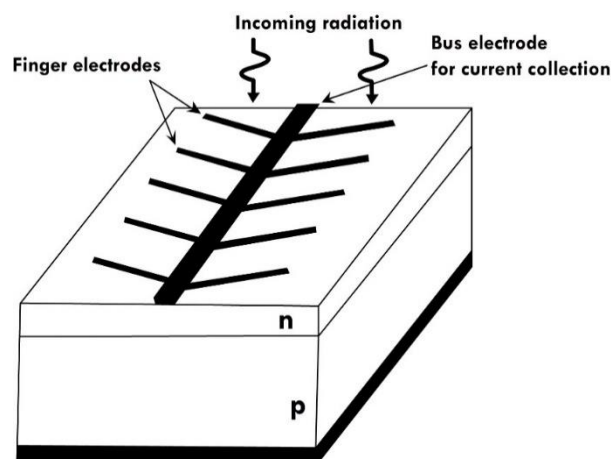

Figure 11 : Finger electrodes on a pn junction solar cell. The design consists of a single bus electrode for carrying current and finger electrodes that are thin enough so that sufficient light can be absorbed by the solar cell. Adapted from Principles of Electronic Materials - S.O. Kasap
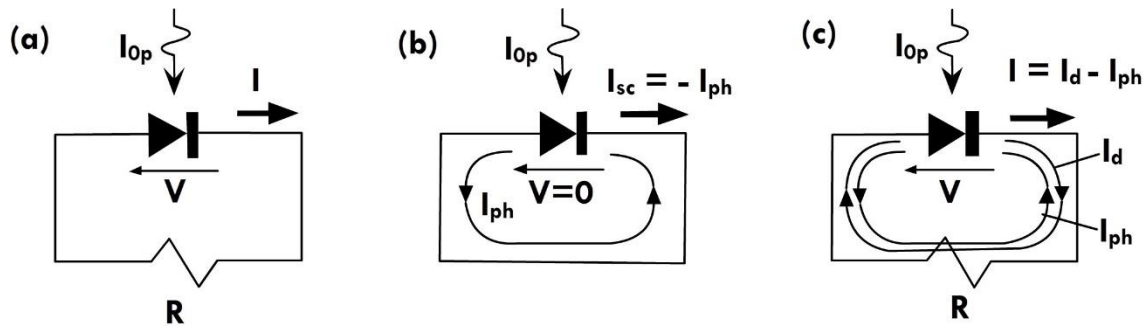
Figure 12 : (a) pn junction solar cell under illumination with an external load. The equivalent circuit (b) without and (c) with an external load. The illumination causes a photocurrent to flow through the external circuit. When an external load is applied the potential drop across it creates a forward bias current that opposes the photocurrent. Adapted from Principles of Electronic Materials - S.O. Kasap

Solar cell I-V characteristics

It possible to calculate the I-V characteristics of the solar cell by considering   its equivalent circuit. The I-V characteristics depend on the intensity of the incident radiation and also the operating point (external load) of the cell. Consider a pn junction solar cell under illumination, as shown in Figure 12. If the external circuit is a short circuit (external load resistance is zero) then the only current is due to the generated EHPs by the incident light. This is called the photocurrent, denoted by I_{ph}. Another name for this is the short circuit current, I_{sc}. By definition of current, this is opposite to the photo current and is related to the intensity of the incident radiation, I_{op}, by

$$I_{sc} = -I_{ph} = -kI_{op} \tag{3}$$

Where k is a constant and depends on the particular device. k is equivalent to an efficiency metric that measures the conversion of light into EHPs.

Consider the case when there is an external load R, as shown in Figure 12. The equivalent circuit for this case is shown in Figure 13 There is a voltage across the external load, given by V=IR. This voltage opposes the built in potential and reduces the barrier for carrier injection across the junction. This is similar to a pn junction in forward bias, where the external bias causes injection of minority carriers and increased current. This forward bias current opposes the photo current generated within the device due to the solar radiation. This is because I_{ph} is generated due to electrons going to the n side and holes to the p side due to

the electric field within the device,

    i.e. Drift current while the forward bias current is due to diffusion current
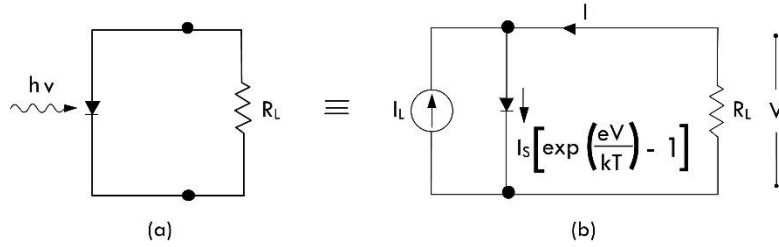

(a)   (b)

Figure 13 : (a) A solar cell connected to an external load (b) Equivalent circuit, with a constant current source, a forward biased pn junction and the external load. The current from the forward biased pn junction opposes the constant current source.

Caused by the injection of minority carriers. Thus, the net current can be written as

$$I_d = -I_{ph} + I_d \tag{4}$$

$$I_d = I_{s0}\left[\exp\left(\frac{eV}{k_BT}\right) - 1\right] \tag{5}$$

$$I = -I_{ph} + I_{s0}\left[\exp\left(\frac{eV}{k_BT}\right) - 1\right]$$

Where I_d is the forward bias current and can be written in terms of the reverse saturation current, I_{s0} and external voltage, V. The overall I-V characteristics is plotted in Figure 14. In the absence of light, the dark characteristics is similar to a pn junction I-V curve. The presence of light (I_{ph}) has the effect of shifting the I-V curve down. From Figure 14it is possible to define a photo current I_{ph}, which is the current when the external voltage is zero and an open circuit voltage, V_{oc}, which is the voltage when the net current in the circuit is zero. Using equation(4), V_{oc} can be calculated as

$$I_{ph} = I_{s0}\left[\exp\left(\frac{eV}{k_BT}\right) - 1\right] \tag{6}$$

$$V_{oc} \approx \frac{k_BT}{e}\ln[\frac{I_{ph}}{I_{s0}}]$$

Higher the photon flux, higher is the value of I_{ph} (by equation (3)) and higher the value of V_{oc}. Similarly, lower I_{s0} can also cause higher V_{oc}. Since I_{s0} is the reverse saturation current for the

pn junction it is given by

$$I_{s0} = n_i^2 e \left[\frac{D_e}{L_e N_A} + \frac{D_h}{L_h N_D} \right] \tag{7}$$
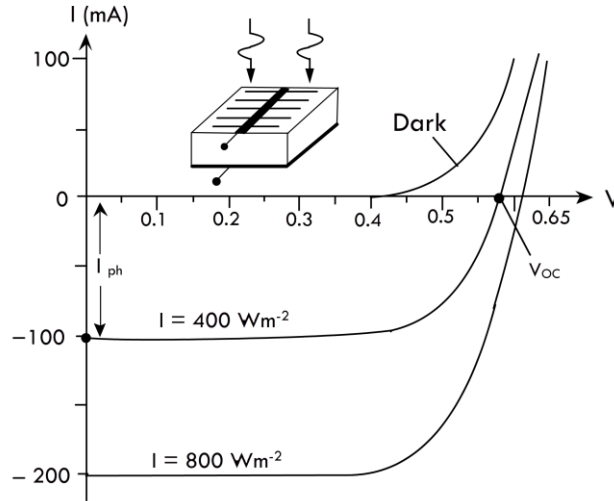

I (mA)

Figure 14 : I - V characteristics of Si pn junction solar cell under dark conditions and under illumination with light of increasing intensity. Short circuit current and open circuit voltage both increase with increasing illumination. Adapted from Principles of Electronic Materials - S.O. Kasap

The reverse saturation current can be lowered by choosing a material with a higher band gap, Eg, which will cause n_i to be lower. But this will also reduce the range of wavelengths that can be absorbed by the material, which will have the effect of lowering I_{ph}. The total power in the solar cell circuit is given by

$$P = IV = I_{s0} V \left[\exp\left(\frac{eV}{k_B T} \right) - 1 \right] - I_{ph} \tag{8}$$

For maximum power, its derivative with respect to voltage should be zero. This gives a recursive relation in current and voltage.

$$\frac{dP}{dV} = 0$$

$$I_m \approx I_{ph} \left(1 - \frac{k_B T}{eV_m} \right) \tag{9}$$

$$V_m \approx V_{oc} - \frac{k_B T}{e} \ln\left(1 + \frac{eV_m}{k_B T} \right)$$

$$P_m = I_m V_m \approx I_{ph} \left[V_{oc} - \frac{k_B T}{e} \ln \left(1 + \frac{e V_m}{k_B T} \right) - \frac{k_B T}{e} \right]$$

This can be seen from Figure 15. The area under the curve, corresponding to I_m and V_m, gives the maximum power. From equation (9) it can be seen that the maximum power is directly proportional to V_{oc} and can be increased by decreasing I_{s0}. This means that smaller n_i and a larger E_g are favourable but the trade-off is that less radiation is absorbed.

Solar cell materials and efficiency

Conventional solar cells are made of Si single crystal and have an efficiency of around 22-24%, while polycrystalline Si cells have an efficiency of 18%. A schematic representation of such a cell is shown in Figure 11. The efficiency of the solar cell depends on the band gap of the material and this is shown in Figure 16. Polycrystalline solar cells are cheaper to manufacture but have a lower efficiency since the microstructure introduces defects in the material that can trap carriers. Amorphous solar cells have an even lower efficiency but can be grown directly on glass substrates by techniques like sputtering so that the overall cost of manufacturing is lowered. There are also design improvements in the solar cell that can enhance the efficiency. PERL (passivated emitter rear locally diffused) cells, shown in figure 12, have an efficiency of 24% due to the inverted pyramid structure etched on the surface that enhances absorption.
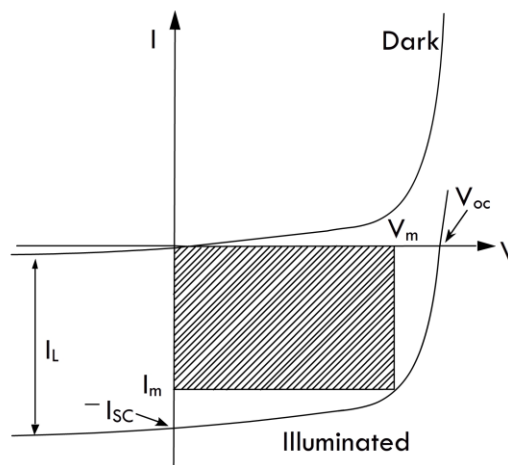
Figure 15 : I-V curve for a solar cell with maximum power indicated by the shaded area. The corresponding voltage and current are Vm and Im. The value depends on the external load applied. Adapted from Physics of semiconductor devices - S.M. Sze.
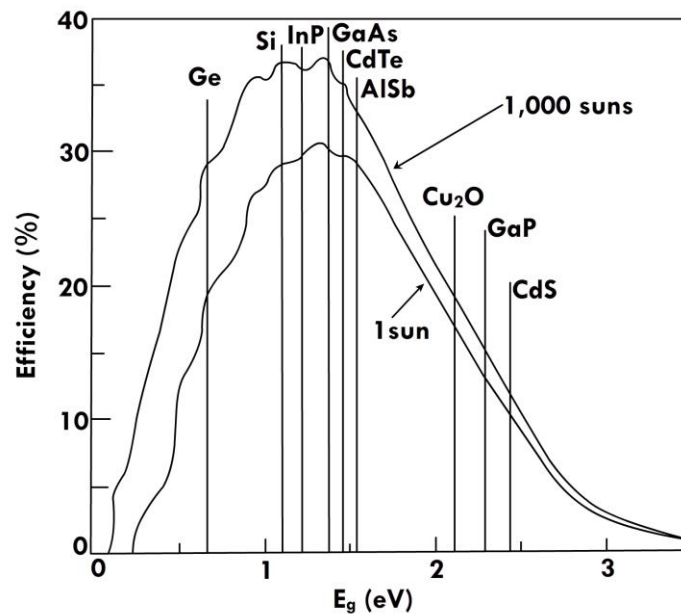

Figure 16 : Solar cell efficiency as a function of band gap of the semiconductor material. There is a particular band gap range where the efficiency is maximum. Adapted from Physics of semiconductor devices - S.M. Sze.
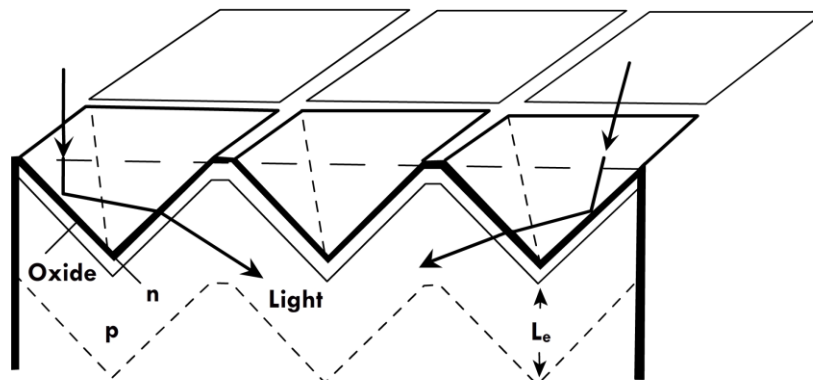

Figure 17 : Si solar cell with an inverted pyramid structure to enhance absorption of the incoming radiation. These are called PERL cells. The inverted pyramid structure causes multiple reflections at the surface, which help in absorption of the incoming radiation. Adapted from Principles of Electronic Materials - S.O. Kasap

Typical solar cells are made of the same material so that the pn junction is a homojunction. Some solar cell materials and their efficiencies are summarized in table 1. A

comprehensive state of current research in different solar cell technologies and their efficiency is available in Figure 18. Heterojunction solar cells are also possible and they have the advantage of minimizing absorption in regions other than the depletion region, but overall cost increases because of the use of different materials and the tight processing conditions needed to produce defect free interfaces. A schematic of such a cell based on GaAs/AlGaAs is shown in Figure 19. The shorter wavelengths are absorbed by the AlGaAs layers while the longer wavelengths, with higher penetration depths, are absorbed by the GaAs layer. This leads to an overall efficiency of around 25%, see table 1. It is also possible to have a homojunction solar cell but with a passivating layer of another material at the surface to reduce defects. This is shown in Figure 20. The surface passivating layer removes the dangling bonds and minimizes carrier trapping. The passivation layer is a thin layer of a higher band gap material to minimize absorption. Similarly, amorphous semiconductor materials like Si and Ge also have a passivating layer of H, a-Si: H or a-Ge: H, to reduce dangling bonds. Another way of improving solar cell efficiency is to have more than one cell in tandem. These are called tandem solar cells and a schematic is shown in Figure 21. These consist of two pn junction solar cells, with the first one having a higher band gap than the second. Thus, the shorter wavelengths can be absorbed in cell 1, see Figure 21, while the longer wavelengths are absorbed in cell 2. The advantage is that a larger portion of the solar radiation is used so that tandem cells have high efficiency, see table1, but it also adds a layer of complexity in growth and increases cost. Tandem cells can also be made using amorphous Si:H and Ge: H. These are cheaper to make and more efficient than individual amorphous solar cell devices.[33]

Table 4 : Some common solar cell materials and their characteristics. Adapted from Principles of Electronic Materials - S.O. Kasap

Semiconductor	Eg (eV)	Voc (V)	Jsc(mA cm^{-2})	η (%)	Comments
Si, single crystal	1.1	0.55-0.7	42	16-24	Single crystal, PERL
Si, polycrystaline	1.1	0.5-0.65	38	12-19	
Amorphous Si:Ge:H film				8-13	Amorphous films with tandem structure, large-area fabrication
GaAs,Single crystal	1.42	1.02	28	24-25	
GaAIAs/GaAs,tandem		1.03	27.9	25	Different band gap materials\ in tandem increases absorption efficiency
GaInP/GaAs,tandem		2.5	14	25-30	Different band gap materials in tandem increases absorption efficiency
CdTe,Thin film	1.5	0.84	26	15-16	

InP, single crystal	1.34	0.87	29	21-22
CuInSe$_2$	1.0			12-13

Figure 18 : Efficiency of various research solar cells. The latest diagram is available at http://www.nrel.gov/ncpv/
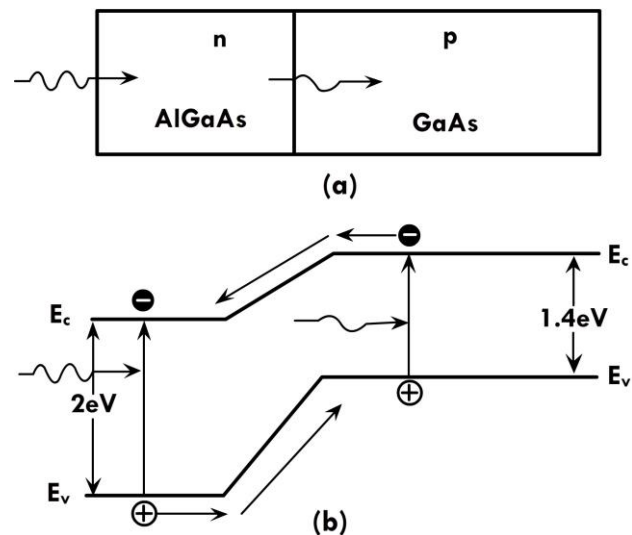
Figure 19 : (a) GaAs/AlGaAs based heterojunction solar cell. (b) Energy band alignment across the junction. AlGaAs has the higher band gap and can absorb higher energy radiation while GaAs can absorb the lower energy portion of the solar spectrum. Adapted from Principles of Electronic Materials - S.O. Kasap
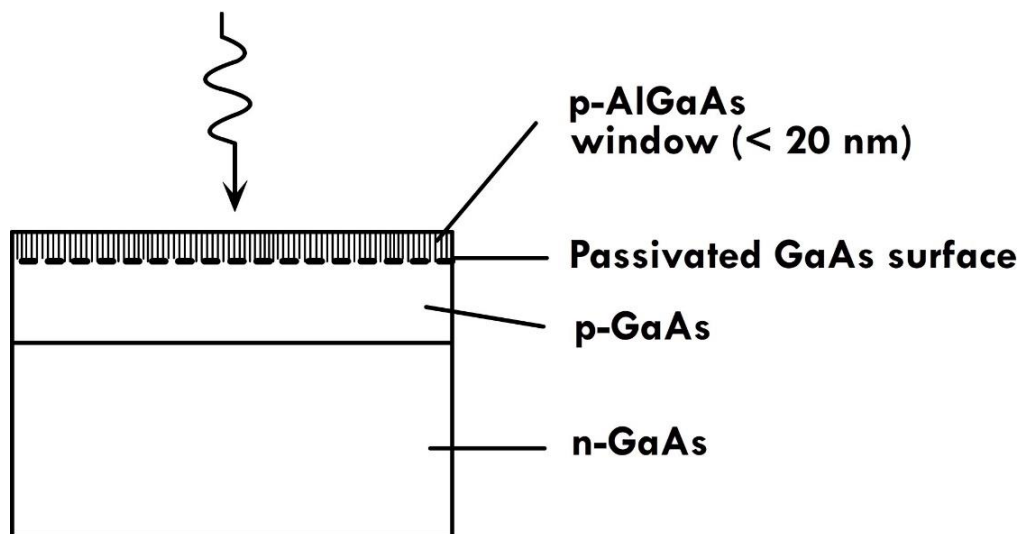

Figure 20 : Schematic of a GaAs based homojunction solar cell with a sur- face passivating layer to minimize surface recombination. This layer should be thin and have a high band gap to minimize absorption. Adapted from Principles of Electronic Materials - S.O. Kasap
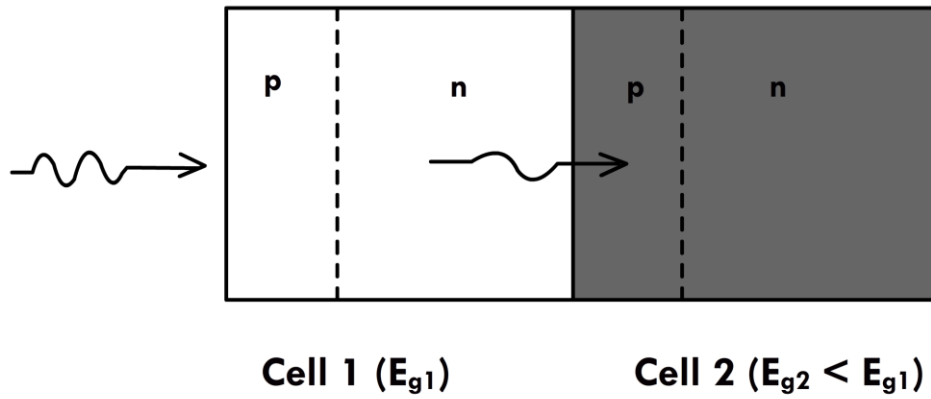
Figure 21 : Tandem solar cells. The higher band gap cell is closer to the illuminating surface to absorb the short wavelengths and the smaller band gap cell is at the interior to absorb the longer wavelengths. Adapted from Principles of Electronic Materials - S.O. Kasap[33]

Materials and Methodology

SCAPS-1D Numerical Simulation.

Understanding the fundamentals of solar cells is made simpler through numerical modelling, which also provides valuable insights into determining the key factors that control the device's performance. One-dimensional equations governing the semiconductor material characteristics under steady-state circumstances can be numerically solved using Solar Cell Capacitance Simulator One Dimension (SCAPS-1D) software. Poisson's equation (10) describes the correlation between the electric field (E) and the space charge density (ρ) of a p−n junction as given below

$$\frac{\partial^2 \Psi}{\partial x} = \frac{\partial E}{\partial x} = \frac{\rho}{\varepsilon_s} = -\frac{q}{\varepsilon_s}[pn + N_D^+(x) - N_A^-(x) \pm N_{def}(x)] \qquad (10)$$

where n(p) refers to the electron (hole) density, N_{def} stands for the potential defect (donor or acceptor) density, and N^+ (N^-) stands for the ionized donor (acceptor) density, q denotes the elementary electronic charge, ψ stands for the electrostatic potential, and ε_s stands for the static relative permittivity of the medium.[34]

Equations (11) and (12) represent the electron and hole continuity in a steady state

$$\frac{\partial j_n}{\partial x} + G - U_n(n, p) = 0 \qquad (11)$$

$$-\frac{\partial j_P}{\partial x} + + G_P - U_P(n, p) = 0 \qquad (12)$$

Here, j_n/j_P stands for the electron/hole current density; G stands for the electron−hole generation rate, and Un,p stands for the rate of net recombination. The density of the electron and hole current is written using equns (13) and (14)

$$j_n = qn\mu_n E + qD_n \frac{\partial n}{\partial x} \qquad (13)$$

$$j_P = qp\mu_P E - qD_P \frac{\partial n}{\partial x} \qquad (14)$$

Where the electron/hole mobility is denoted by $\mu_{n/}$, and the diffusion is denoted by D

Table 5 TCO, ETLs, CBTS HTL, and Cs_2BiAgI_6 Absorber Layer's Initial Input Parameters[35][36]

Parameters	ITO	TiO$_2$	CBTS	Cs$_2$BiAgI$_6$
Thickness (nm)	500	30	100	800[a]
Band gap, E$_g$ (eV)	3.5	3.2	1.9	1.6
Electron affinity, X (eV)	4	4	3.6	3.90
Dielectric permittivity (relative), ε_r	9	9	5.4	6.5
CB effective density of states, N$_c$ (1/cm^3)	2.2×10^{18}	2×10^{18}	2.2×10^{18}	1×10^{19}
VB effective density of states, N$_V$ (1/cm^3)	1.8×10^{19}	1.8×10^{19}	1.8×10^{19}	1×10^{19}
Electron mobility, μ_n (cm^2/Vs)	20	20	30	2
Hole mobility, μ_h (cm^2/Vs)	1×10^{21}	10	10	2
Shallow uniform acceptor , N$_A$ (1/cm^3)	0	0	1×10^{18}	1×10^{15a}
Shallow uniform donor density, N$_D$ (1/cm^3)	1×10^{21}	9×10^{16}	0	0

| Defect density, N_t $(1/cm^3)$ | 1×10^{15a} | 1×10^{15} | 1×10^{15a} | 1×10^{15a} |

To obtain the optimal HTL, ETL, and back contact metal combination in this study, these variables are kept constant during the first optimization

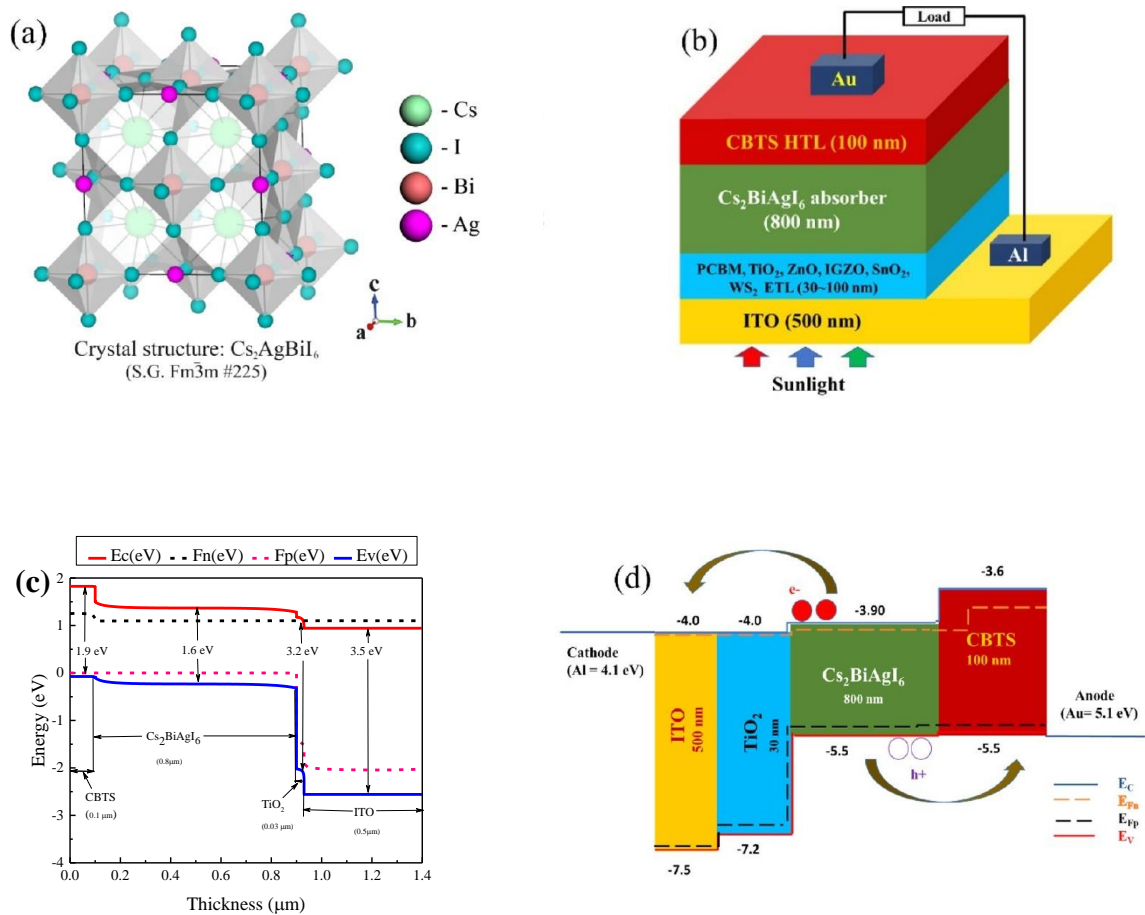## Cs$_2$BiAgI$_6$ Perovskite Solar Cell Structure.

Figure 22: (a) Crystal structure of the absorber (b) device structure (c) band diagram and (d) energy band alignment of an optimized solar cell structure

In this study, the simulation was performed on SCs with an n-i-p planar heterojunction structure comprising the ETL, Cs$_2$BiAgI$_6$ absorber Figure (10)a, HTL, transparent conduction oxide

(TCO), represent the p-region, i-region, and n-region, respectively. The absorber layer (Cs_2BiAgI_6) of the solar cell creates excitons when it is exposed to light. The exciton is a restricted state made up of an electron and a hole. The exciton can penetrate the n (p) area based on the length of the diffusion. The exciton separates at the n-to-i-layer interface, and the e^- and remaining holes are sent toward the direction of the n-layer and p-layer, successively. Similarly, the exciton separates at the i-to-p-layer interface, and the holes and remaining e^- are sent in opposite directions, toward the p-layer and the n-layer. The electrical field that exists between these layers allows the separation of excitons and also the movement of e^- and holes. As a TCO, indium tin oxide (ITO) is employed, with a work function of 4.4 eV. Assumed to be 500 nm in thickness is the TCO layer.

Table 6. Interface Defect Layers' Input Parameters[35]

Interface	Defect type	Capture cross section: electrons/holes(cm^2)	Energetic distribution	Reference for defect energy level	Total density (cm^{-3}) (integrated over all energies)
ETL/Cs_2Bi AgI_6	neutral	1.0×10^{-17} 1.0×10^{-18}	single	above the VB maximum	1.0×10^{10}
$Cs_2BiAgI_6/$ HTL	neutral	1.0×10^{-17} 1.0×10^{-18}	single	above the VB maximum	1.0×10^{10}

The thickness of the ETL, HTL, and absorber layers is changed over a wide range to optimize device performance. In this proposed device configuration, The ETLs named TiO_2, PCBM, ZnO, IGZO, SnO_2, and WS_2 are used as ETLs, and CBTS is used as an HTL. In addition, the absorber layer Cs_2BiAgI_6 is sandwiched between the ETL and the HTL in every device structure and serves as the light- absorbing layer. Figure 22b demonstrates the structure of the optimized Cs_2BiAgI_6- based PSCs. Figure 22c represents the band diagram of the Cs_2BiAgI_6-

based PSC device configuration where TiO_2 is used as the ETL along with the CBTS HTL, and the corresponding energy band alignment is shown in Figure 22d. Each ETL with an absorbing layer and CBTS as the HTL are utilized by the energy band diagram to influence the valence band offset. The difference between the absorber layer and HTL represents the valence band. The effectiveness and performance of the PSCs are significantly impacted by the alignment of the energy levels. In the PSCs, holes are simultaneously transferred to CBTS as the HTL while e^- are injected into the corresponding ETL conduction band. After that, holes and e^- are collected at the respective Au (back contact metals) and ITO. However, the electron affinity of each studied ETL should be higher than that of Cs_2BiAgI_6 to extract the electron at the ETL/Cs_2BiAgI_6 interface, and the HTL ionization energy should be lower than that of Cs_2BiAgI_6 to extract the holes at the $Cs_2BiAgI_6/CBTS$ HTL interface. In addition, the solar cell's performance is significantly impacted by the energy band mismatch at the ETL/Cs_2BiAgI_6 and the $Cs_2BiAgI_6/CBTS$ as the HTL. The performance and effectiveness of the optimized six ETL-based double perovskite solar structures are investigated with the help of the input parameters of interface defect layers. In all cases of simulation, a frequency of 1 MHz, AM 1.5 G spectrum of sunlight was used by maintaining the surrounding temperature of 300 K

Results and Discussions

Effect of Absorber, ETL and HTL Layers Thicknesses on PV Performance

Absorber Layer Thickness

The absorber layer thickness plays an important role in affecting the PSC performance through the enhancement in photon absorption and device efficiency. The Cs_2BiAgI_6 absorber layer thickness is varied from 0.1 to 1.5 μm to optimize the device performance. The variation of V_{OC}, J_{SC}, FF, and PCE is demonstrated for the ten sets of device configurations while increasing the thickness of the Cs_2BiAgI_6 absorber layer, as shown in Figure 23. V_{OC} decreases with the increasing absorber layer thickness due to the rise in the value of J_{SC} as governed by the equation

$$V_{OC} = \frac{k_B T}{q} \ln[\frac{J_{SC}}{J_0} + 1].[37] \tag{15}$$

J_{SC} initially increased rapidly and then saturated due to the saturation in the number of photons available for absorption. The FF decreased monotonically with an increase in the absorber thickness due to the improved series resistance. The decline in the FF might be due to the dominance of carrier recombination and parasitic resistance losses. As the change in voltage has relatively little impact on the PCE curve, this rise in J_{SC} also explains an increase in PCE. Due to the increase in the recombination rate with the absorber layer thickness, V_{OC} gradually decreases. The PCE initially improved with the absorber thickness and showed peaks at 1000, for TiO_2 ETLs, which ultimately determined the optimum absorber thickness. The initial rise of PCE is due to an increase in the generation of electron - hole pairs as the absorber layer thickness increases. However, the increased radiative recombination and charge route resistance causes a decrease in PCE for thicker absorbers.[35]
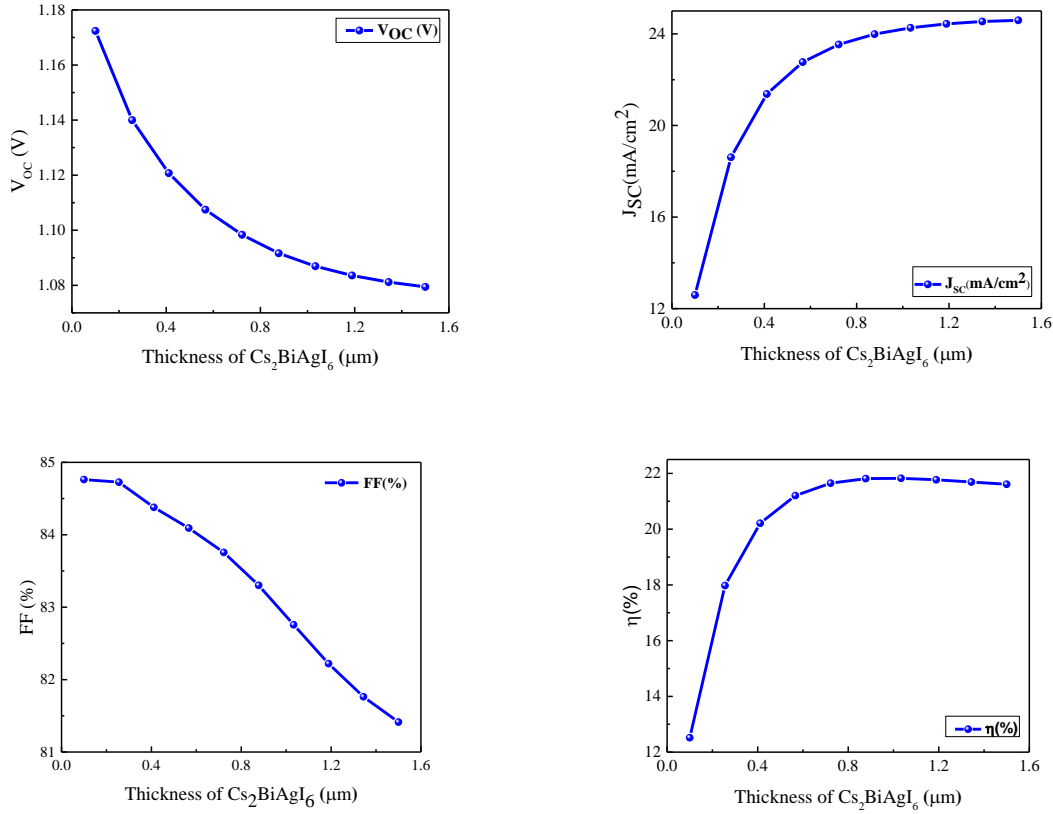
Figure 23 : Effect of the variation in the PV parameters PCE, FF, J_{SC}, and V_{OC} due to the variation in the thickness of the absorber,

ETL (TiO₂) Thickness

The properties of the charge transport layers should be carefully tuned to design highly efficient PSCs. A suitable ETL aids in increasing transmittance and lowering recombination in PSCs. The thicknesses of the TiO₂ as ETLs were varied from 30 to 500 nm while keeping other parameters constant to determine the performance of double PSC. Figure 24 shows that the thickness of the ETL has less impact on the PV performance parameters of Cs_2BiAgI_6-based PSCs. The partial absorption of a thicker ETL slows down the charge generation and collection pace and may cause a slight decline in J_{SC} and PCE. Equn (16) shows the relation between the ETL layer thickness and transmittance.[38]

$$\alpha_e = \frac{1}{d_e} \ln \frac{1}{T_e} \tag{16}$$

Where d_e stands for the film thickness, T_e stands for the transmittance, and α_e denotes the absorption coefficient. However, it is observed from Figure 24 that on increasing TiO₂, V_{OC} remains constant. The J_{SC} value for increasing thicknesses TiO₂, remains constant there is a

decline in the value of J_{SC}. The FF and PCE layers remained constant, as shown in Figure 24 After trial and error, the optimized thickness of TiO_2, is found to be 30nm. The optimum thickness of ETLs helps to achieve the maximum PCE value for the device configurations.
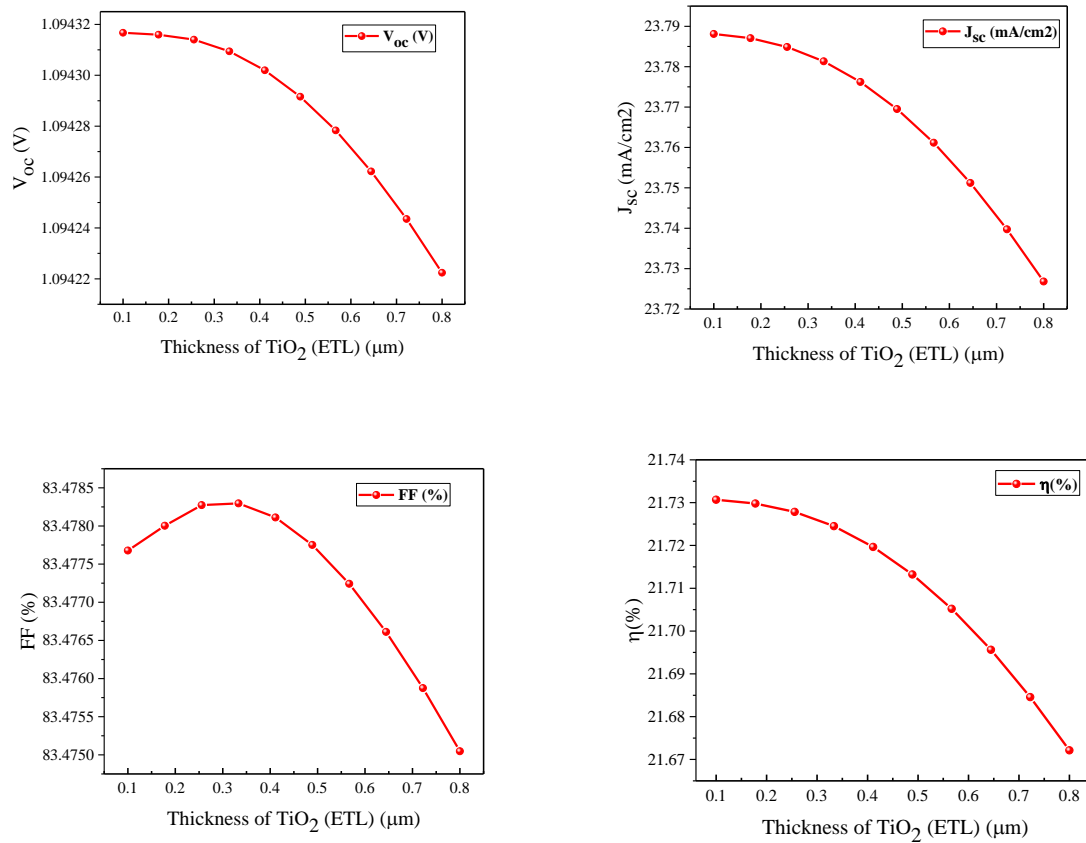

Figure 24: Effect of the variation in the PV parameters PCE, FF, J_{SC}, and V_{OC} due to the variation in the thickness of ETL

HTL Thickness

The impact of changing the thickness of the CBTS HTL on PV parameters in Cs_2BiAgI_6- based PSCs using TiO_2 as ETLs are shown in Figure 25. HTL thickness modification is crucial to maximize performance and minimize direct contact between the perovskite and cathode. This layer also serves as a capping layer. We examine only CBTS as the HTL in thickness optimizations because only CBTS exhibited a maximum PCE Figure 25 shows that the values of V_{OC}, J_{SC}, FF, and PCE remained constant for all ETLs with increasing thickness of CBTS as the HTL. The V_{OC} value decreases around 1.10 V for TiO_2 for the increased thickness of CBTS. The FF and PCE values of TiO_2 at around 83.3 and 21.68%, respectively, are the highest among the ETL. It has been observed in the previous study that the PCE value increased with

38

increasing HTL thickness.[39] Typically, a p-type layer must be thicker than an n-type layer to reduce the recombination rate because it aids in the efficient prompt transportation of equivalent charge carriers to the respective terminals.[40] But during the variation of HTL thickness, 100 nm is observed to be the best thickness for a higher PCE, and hence 100 nm is chosen as the optimized HTL thickness for further calculations.
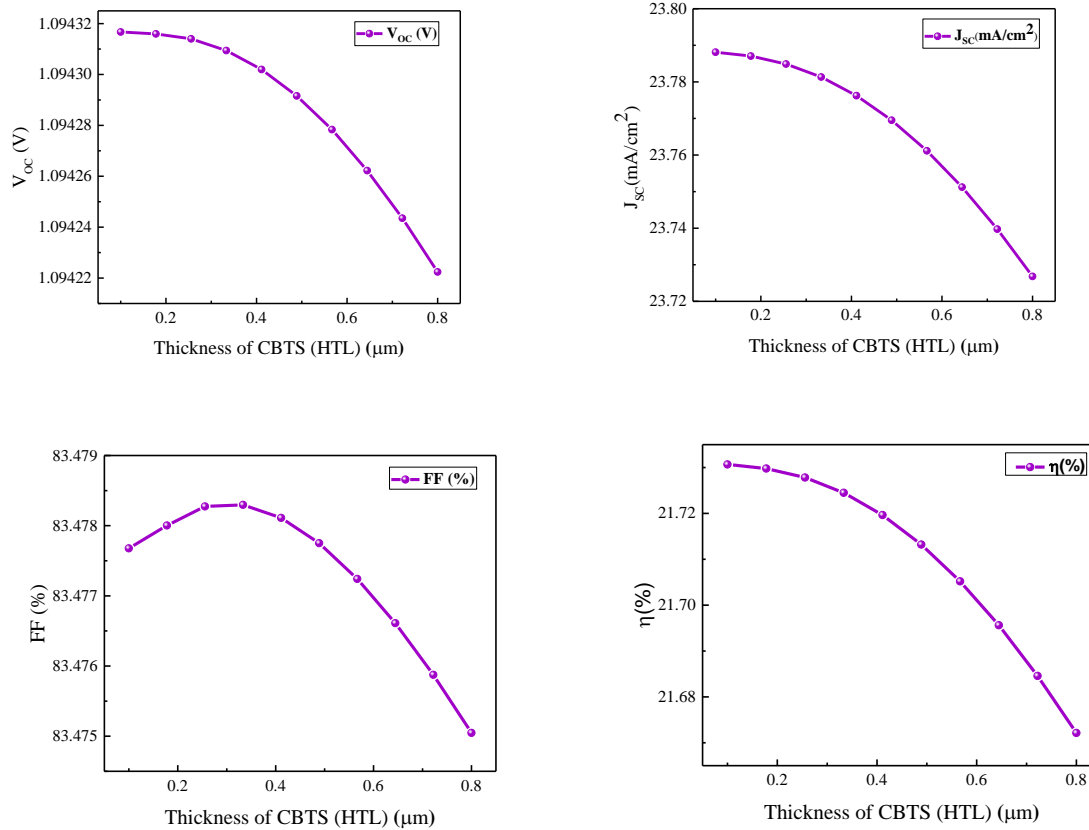

Figure 25 : Effect of the variation in the PV parameters PCE, FF, J_{SC}, and V_{OC} due to the variation in the thickness of HTL TiO_2 as ETL.

Effect of Absorber Layer Properties.

Absorber Layer Acceptor Density.

Electron−hole pairs are produced as a result of the incoming radiation's photons being absorbed by the perovskite absorber layer. To enhance the performance of SCs, a little amount of n-type or p-type dopants may be added to the perovskite absorber layer.[41] Here, in this section, the N_A of the absorber is changed from 10^{10} to 10^{17} cm^{-3} to see its impact on the PV

parameters. Figure 26 shows that the V_{OC} for the optimized ETL is constant for N_A values up to 10^{14} cm^{-3}, and thereafter V_{OC} increases with the N_A. When N_A rises, the Fermi energy level of the holes decreases, which increased the V_{OC} level. As the absorber layer N_A rises, the built-in potential also increases; this may contribute to the rise in V_{OC} brought on by the increased charge separation. The PCE value decreases when the N_A value exceeds 10^{17} cm^{-3} of optimized SC structures. In addition, the PCE also decreases when the defect states rise with the increase in N_A. All of the PV parameters V_{OC}, J_{SC}, FF, and PCE remained constant till 10^{17} cm^{-3}; hence, the ideal N_A for better performance can be between 10^9 and 10^{17} cm^{-3}. As the absorber N_A increases, an electric field is generated at the interface layers of the PSC. However, the creation of the electric field also makes the possibility of charge carrier recombination conceivable. Therefore, the ideal acceptor doping density should be selected to produce higher performance. Finally, the optimized N_A of the absorber layer for TiO$_2$ ETL is set at 10^{15} cm^{-3}.
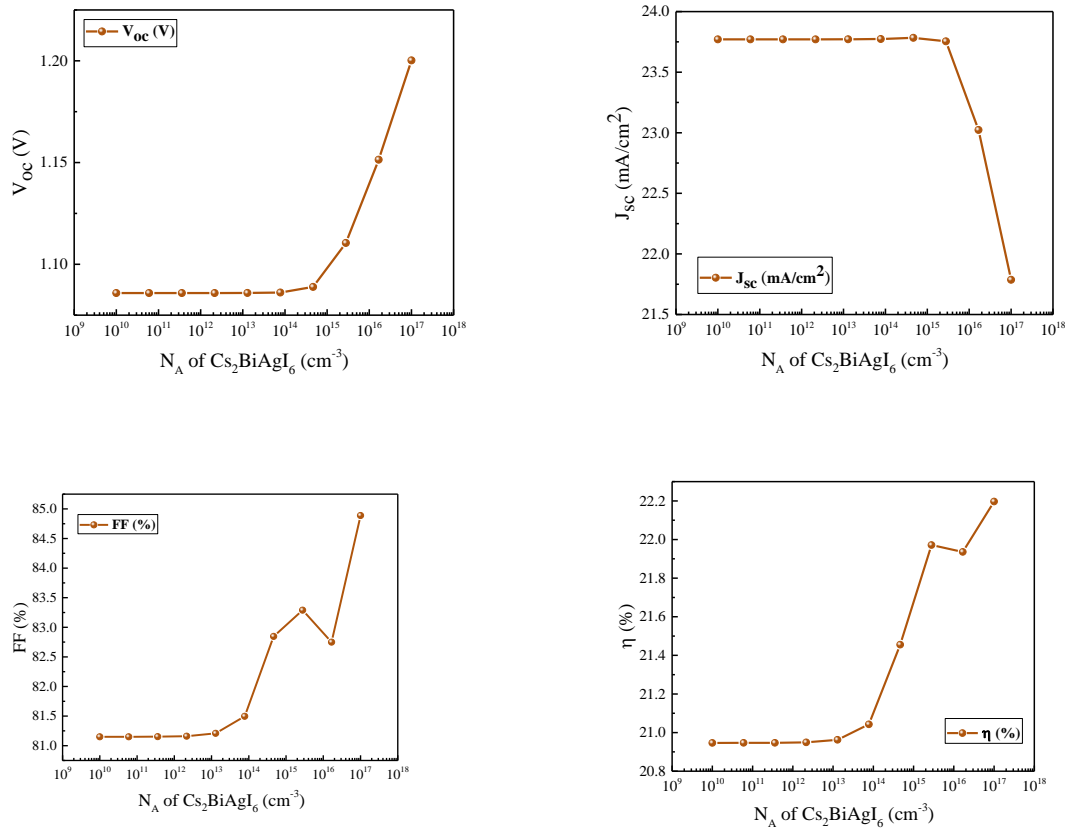

Figure 26 : Effect of the variation in the PV parameters PCE, FF, J$_{SC}$, and V$_{OC}$ due to the variation in the thickness of HTLs TiO2 as ETLs.

The absorber layer defect density

N_t is a critical factor in determining the effectiveness and performance of PSCs. The properties of the light-absorbing layer and its form significantly influence the PCE of PSCs. When light is incident on the perovskite absorber layer, photo carriers are produced. However, a poor morphology of the ETL could lead to insufficient perovskite layer coverage. A lower-quality film has higher N_t, which raises the recombination rate.[42]. N_t of the ETL was changed from 10^9 to 10^{18} cm^{-3} for Cs$_2$BiAgI$_6$- based structures. Figure 27 shows that the V_{OC}, J_{SC}, FF, and PCE values are constant till 10^{14} cm^{-3} of N_t. Beyond the N_t value of 10^{14} cm^{-3}, the PV parameters are reduced for TiO$_2$, ETL. According to the earlier literature, this declination in PV parameters with an increase in N_t happened due to the nonradiative Shockley− Read−Hall (SRH) recombination, which is also the main reason for carrier recombination, lifespan reduction, and a decline in the PSC performance.42 Figure 11b shows that the PCE for Cs$_2$BiAgI$_6$-based PSCs is about 22%, and for N_t of 10^{18} cm^{-3}, the PCE is reduced to about 1%. The existence of several kinds of recombination mechanisms, such as trap-aided SRH recombination and interface recombination in PSCs, is primarily responsible for this significant degradation in the PCE. The SRH recombination rate is defined using eqs (17) and (18)

$$R_{SRH} = [nP - n_i^2]/[\tau(P + n + \frac{2n_i \cosh(E_i - E_t)}{kT})] \tag{17}$$

$$\tau = 1/[\sigma \times N_t \times V_{th}] \tag{18}$$

(17) (18) where σ stands for the capture cross section of electrons and holes, Et stands for the defect energy level, E_i stands for the intrinsic energy level, n_i is the intrinsic carrier concentration, n/p is the concentration of electrons/holes, τ stands for the lifetime of holes and electrons, V_{th} stands for the thermal velocity of charge carriers, and N_t stands for the total defect density of the absorber layer of the PSC. The optimized N_t for TiO$_2$ is fixed, to 10^{12} cm^{-3}, for the maximum PCE using the trial-and-error method.
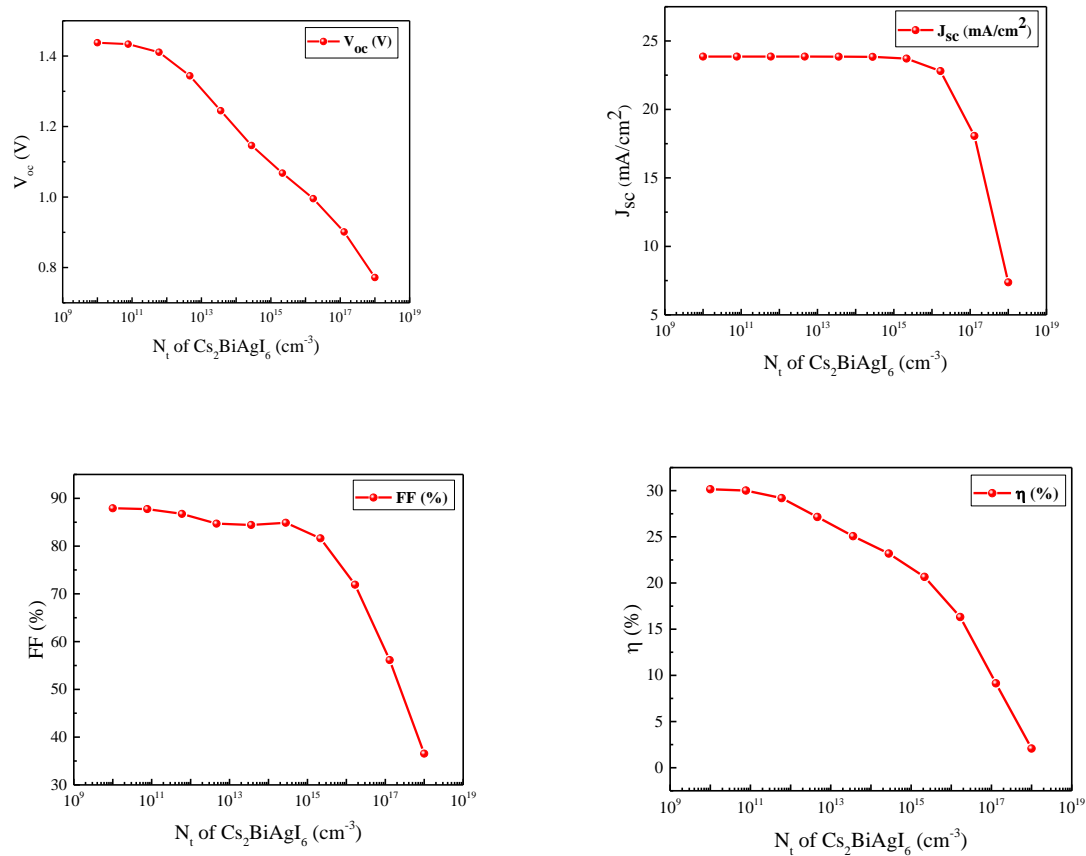
Figure 27 : Effect of the variation of the defect density of the absorber layer for ETL

Effect of ETL properties.

ETL Donor Density.

The changes of PV parameters, such as V_{OC}, J_{SC}, FF, and PCE, versus doping concentration (N_D) of TiO_2 as ETL, are shown in Figure 28 N_D of ETL was changed from 10^{10} to 10^{19} cm^{-3} Figure 28 The V_{OC} value remained constant with N_D for ETL. On increasing N_D, TiO_2 showed a V_{OC} value of around 1.12 V. J_{SC} values for TiO_2 remained constant with N_D. The FF of ZnO decreases with an increasing value of N_D of the ETL. The remaining ETL maintains a constant FF value with the change of N_D. TiO_2 exhibit a constant PCE profile with increasing N_D. However, ETL show a small rise in FF and PCE with increasing N_D because a higher value of the N_D of the ETL makes charge extraction and transmission at the ETL/ Cs_2BiAgI_6 contact more feasible. Due to the large series resistance at the lower N_D of the ETL,

the performance of the PSC degrades.[43][44] The optimum N_D of TiO_2 is set at 9×10^{17} cm^{-3} for further optimization.
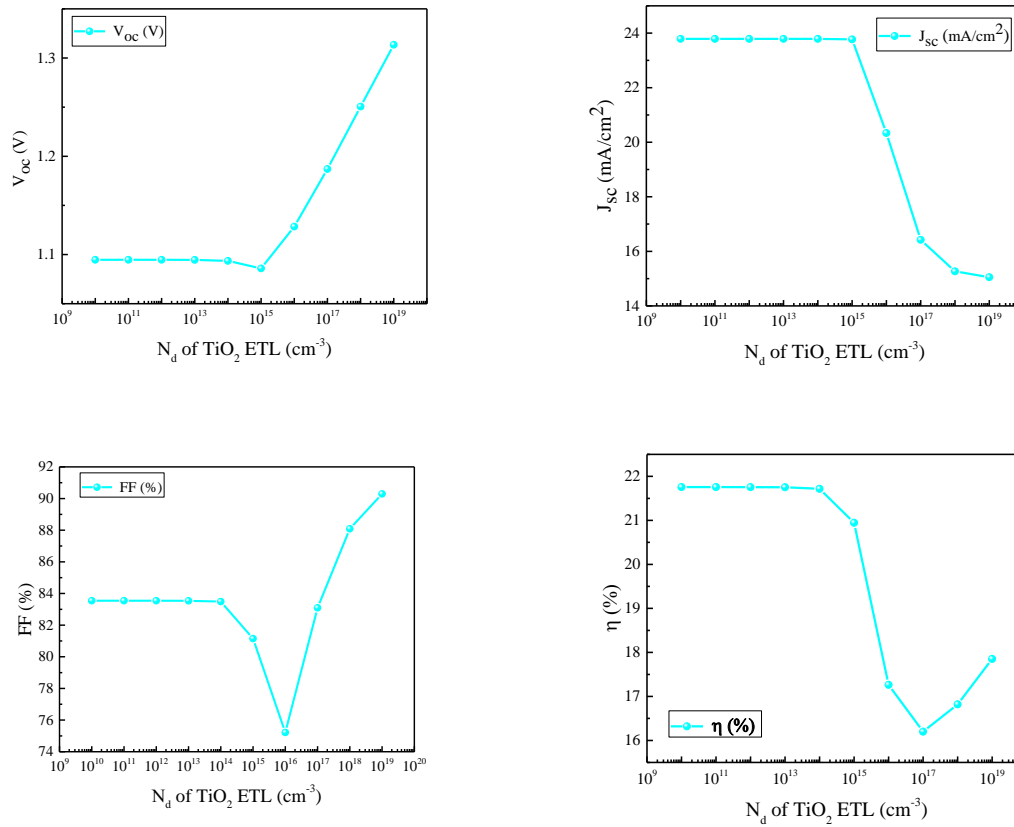

Figure 28 : Effect of the variation of the donor density of ETL

Effect of ETL Defect Density.

V_{OC}, J_{SC}, FF, and PCE values are computed for different ETLs by increasing ETL N_t from 10^{10} to 10^{17} cm^{-3}. Figure 29 showed that almost all performance parameters V_{OC}, J_{SC}, FF, and PCE exhibited constant values for ETL layers on increasing N_t of the ETL. ETL showed a V_{OC} value of around 1.09 V. ETL layer showed a J_{SC} value of around 24 mA/cm^2. The FF value of the ETL layer remained constant which showed a slight decrease after 10^{16} cm^{-3}. the PCE of 23.5% is achieved with TiO_2. From the simulated data, the optimized N_t of the ETL is 10^{15} cm^{-3} PSC structures.
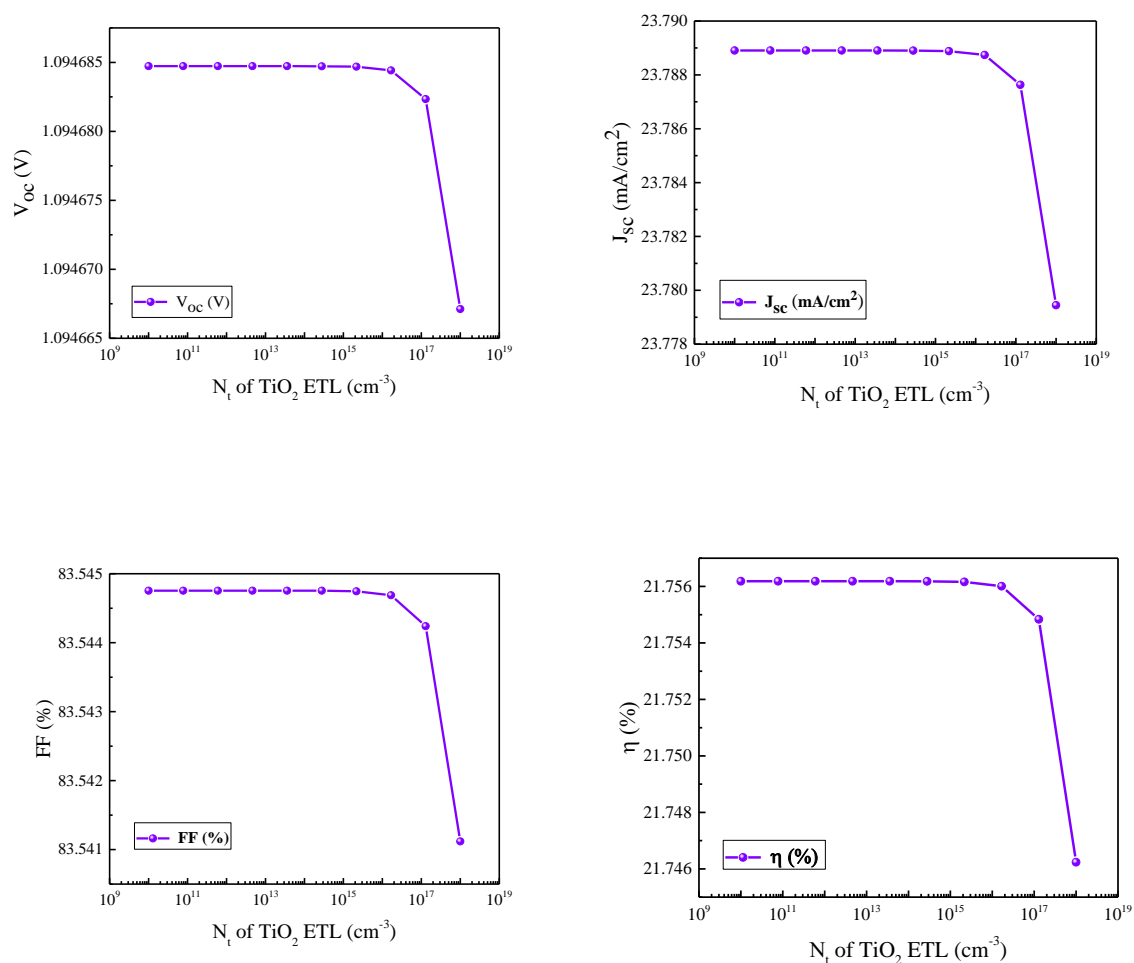
Figure 29 : Effect of the variation of the defect density of the ETL.

Effect of HTL properties.

HTL Acceptor Density

Figure 30 shows the change of photo-voltaic parameters with increasing HTL N_A (acceptor concentration) for TiO_2 ETL. N_A is varied from 10^{15} to 10^{21} cm^{-3} for SC structures. From Figure 30 it is evident that PCE values with ETL showed comparatively low values with $N_A <$ 10^{16} cm^{-3} due to the small electric field, which reduces carrier extraction. In addition, on increasing N_A beyond 10^{16} cm^{-3}, a constant PCE value is obtained for device configurations. A similar pattern has been seen for the FF value for all   presented PSCs, where FF increases as N_A from 10^{15} to 10^{16} cm^{-3}. The J_{SC} value for ETL associated with PSCs exhibited a constant

value with an increasing N_A. The constancy indicates that the N_A variation of the HTL has an insignificant impact on J_{SC}. The J_{SC} is observed for TiO_2 associated SC structures is around 24 mA/cm^2. The ETL showed a constant V_{OC} value with N_A variations. Optimum N_A was found to be 10^{18} cm^{-3} for ETL and we fixed the value of N_A for further optimization.
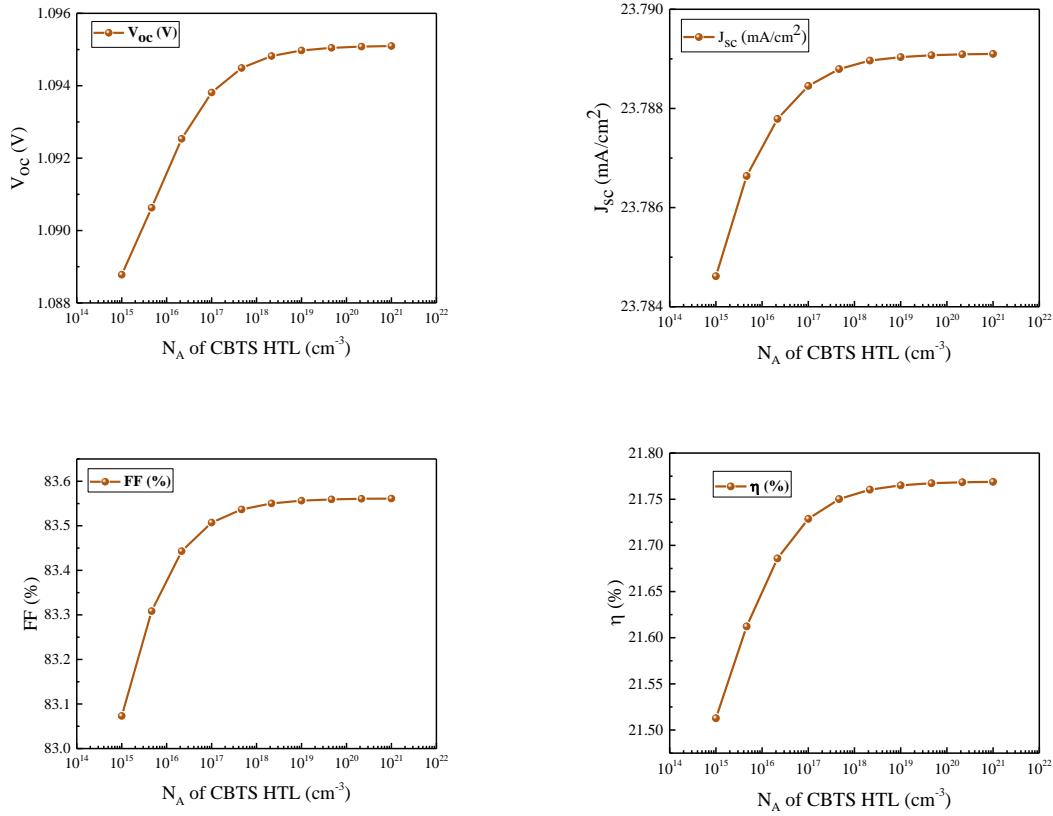

Figure 30 : Effect of the variation of the donor density of the HTLs

HTL Defect Density.

N_t of the HTL in this section varies from 10^{11} to 10^{18} cm^{-3}, as shown in Figure 31. The PCE value of different ETLs remained constant with increasing N_t of the HTL until 10^{17} cm^{-3}. The PCE value decreased sharply after 10^{17} cm^{-3}. Therefore, with increasing N_t, the PCE value has an insignificant impact of Cs_2BiAgI_6-based PSC. The V_{OC} and J_{SC} values remained constant for ETL device configurations on increasing N_t of CBTS as the HTL. Therefore, increasing N_t of CBTS has an insignificant impact on device configurations. The optimized value of N_t is set to 10^{15} cm^{-3} for device structures for further optimization.
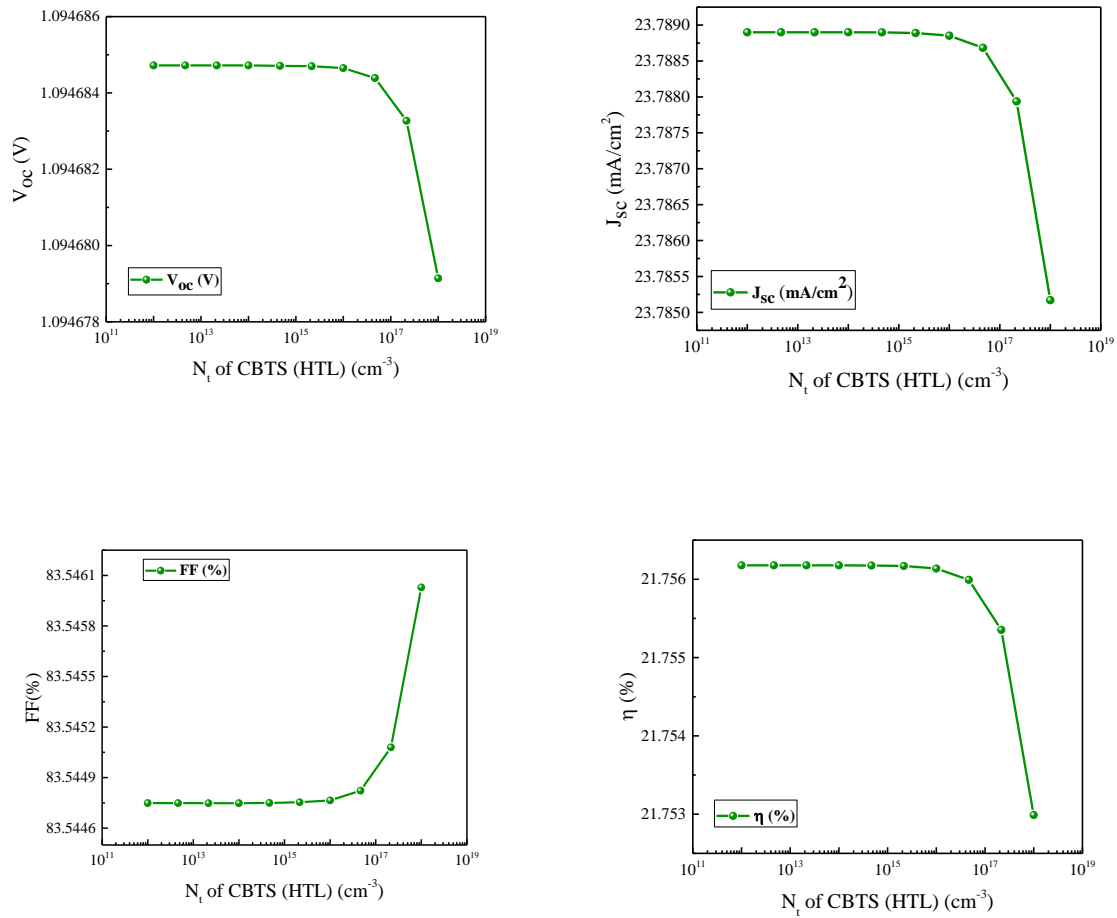
Figure 31 : Effect of the variation of the defect density of the HTLs.

Effect of Interface Properties.

Defect Density at the Interface of HTL and the Cs2BiAgI6 Absorber Layer.

Several defect states frequently coexist at the interface between perovskite and transport material. The performance of the SC depends significantly on the interface quality. According to the earlier study, the interface defect density (N_t) on the irradiation side will affect solar cell performance more than the interface defect states at the rear interface[45]. The performance parameters V_{OC}, J_{SC}, FF, and PCE have been investigated for the change of N_t of the CBTS HTL/Cs_2BiAgI_6 interface from 10^{10} to 10^{22} cm^{-3} for all of the ETLs, as shown in Figure 32. The PCE and FF values exhibited the same declining pattern on increasing the defect density (N_t) of the CBTS HTL/Cs_2BiAgI_6 interface. The maximum values of PCE and FF are exhibited at N_t in the range $10^{10}-10^{14}$ cm^{-3}, and after N_t, of more than 10^{16} cm^{-3}, the PCE and FF values

46

start decreasing. In contrast, ETL with Cs_2BiAgI_6 perovskite exhibited a PCE of more than 22.9% at 10^{10} cm^{-3}. The J_{SC} value with changing N_t remained almost constant. From the simulation data, it is observed that on increasing the defect density, the recombination rate increased, and the PCE value decreased. Increased trap and recombination centres are produced due to higher defect concentrations at the interfaces, which reduces SC performance. The simulation results showed that an ideal N_t for device simulation is 10^{10} cm^{-3}. Therefore, the optimum N_t is set at 10^{10} cm^{-3} for device configurations for further optimization.
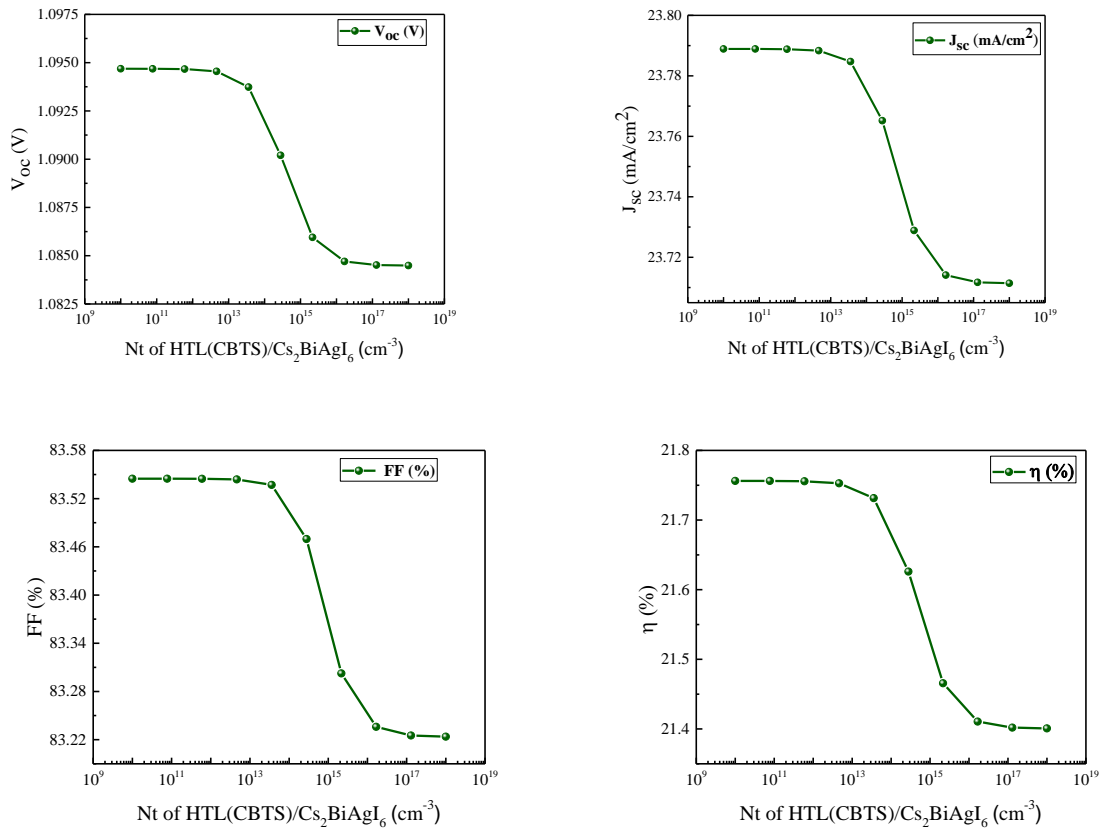

Figure 32 : Effect of the defect density variation of the HTL/Cs_2BiAgI_6 interfaces on PV parameters PCE, FF, J_{SC}, and V_{OC}

Defect Density at the Interface of the Cs2BiAgI6 Absorber Layer and ETL.

The effects of the Cs_2BiAgI_6-ETL interface defect density (N_t) on the effectiveness of gradient doping PSCs are examined in this section. N_t was varied from 10^{10} to 10^{18} cm^{-3}. From Figure 33 it is observed that the value of V_{OC}, J_{SC}, FF, and PCE decreases on increasing the N_t. The PV value remained constant till 10^{14} cm^{-3} and then start decreasing with N_t variations.

47

TiO$_2$ as ETLs for the Cs$_2$BiAgI$_6$ SC structure showed the highest PCE, The FF value of TiO$_2$ after exceeding 10^{15} cm^{-3}, the FF value decreased rapidly. The lowest J$_{SC}$ of 24 mA/cm^2 is exhibited for TiO$_2$. V$_{OC}$ is much more sensitive to the changes in N$_t$ as compared to J$_{SC}$. The formula in eq 10 may be used to describe the interface recombination-imposed V$_{OC}$ limit.[46]

$$V_{oc} = \frac{1}{q}\{\phi_e - nKTln\left(\frac{N_V S_t}{J_{sc}}\right)\} \tag{19}$$

Where S$_t$ is the rate of interface recombination, n is the ideality factor, and ϕ_e is the height of the effective barrier. This formula reveals that a high S$_t$ will be produced by a high interface defect density, which will reduce V$_{OC}$. However, the optimum N$_t$ value is found to be 10^{10} cm^{-3}, which is similar to that obtained in the case of HTL/ Cs$_2$BiAgI$_6$.
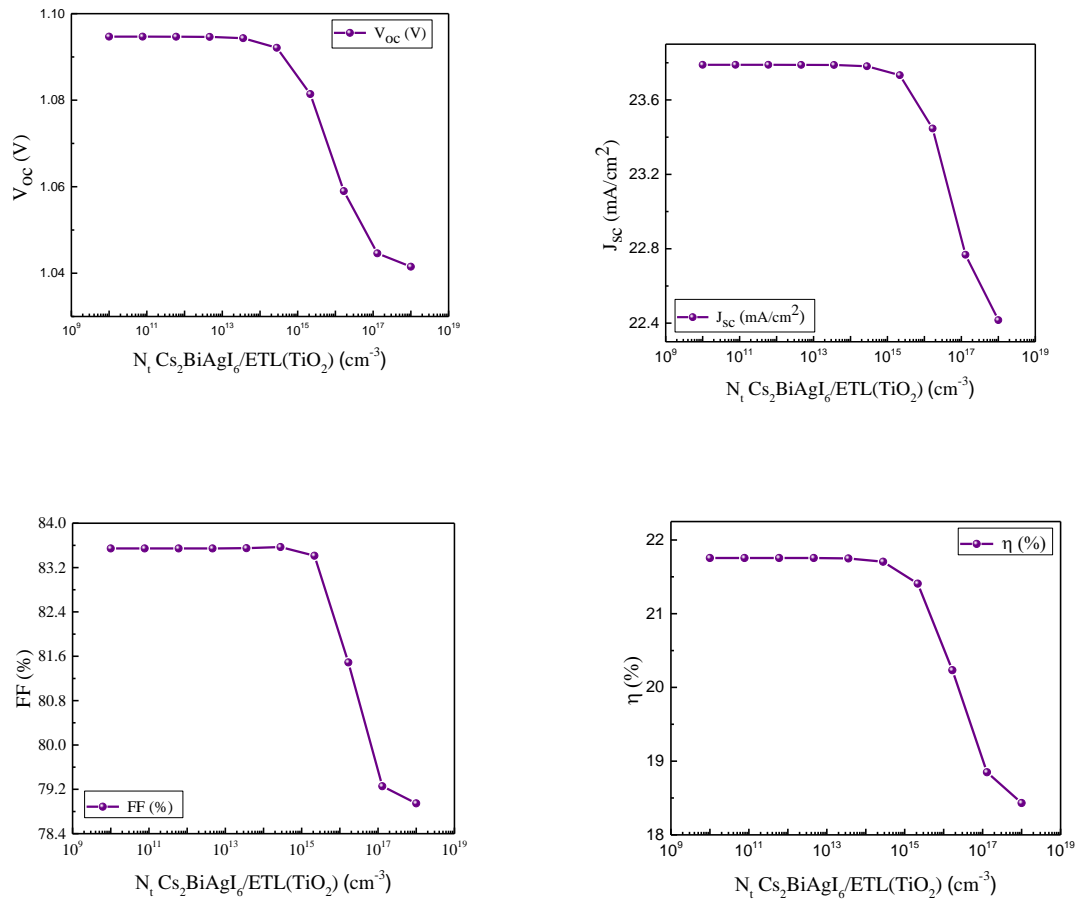

Figure 33 : Effect of the defect density variation of the Cs$_2$BiAgI$_6$/ETL interfaces on PV parameters PCE, FF, J$_{SC}$, and V$_{OC}$.

Effect of Temperature, Shunt, and Series Resistances

Series Resistance

R_S stands for internal resistance, which is made up of the device's active layer resistance and its ohmic contact resistance. According to Figure 34 the effect of the variation of the series resistance from 0 to 8 Ω cm^2, keeping the shunt resistance constant at 10^5 Ω cm^2 for optimized TiO^2 ETL-associated structures, are investigated. It was observed that increasing R_S had no discernible impact on J_{SC} and V_{OC}. The FF and PCE for the structures have, however, significantly decreased as a result of the increase in R_S. This was found to be consistent with the findings for both inorganic and organic solar cells. [47][48] Practically speaking, the value of R_S for solar cells often decreases as a result of aging related effects that cause inconsistent photovoltaic performance. Accordingly, to improve the FF and get the highest performance feasible, R_S must be kept to a minimum value throughout the device's fabrication. One could consider lowering the active layer of a device's thickness during manufacture to lower RS. Nevertheless, reducing the thickness is rarely a good strategy, particularly for perovskite solar cells, since this results in a noncomplementary absorption when the thickness is maintained under 200 nm. Other experimental methods to lower R_S include decreasing the contact resistance between the active layer and electrodes [49] or creating donor−acceptor interfaces that interact well. From Figure 34 the lowest J_{SC} is observed in the case of the TiO$_2$-based ETL.
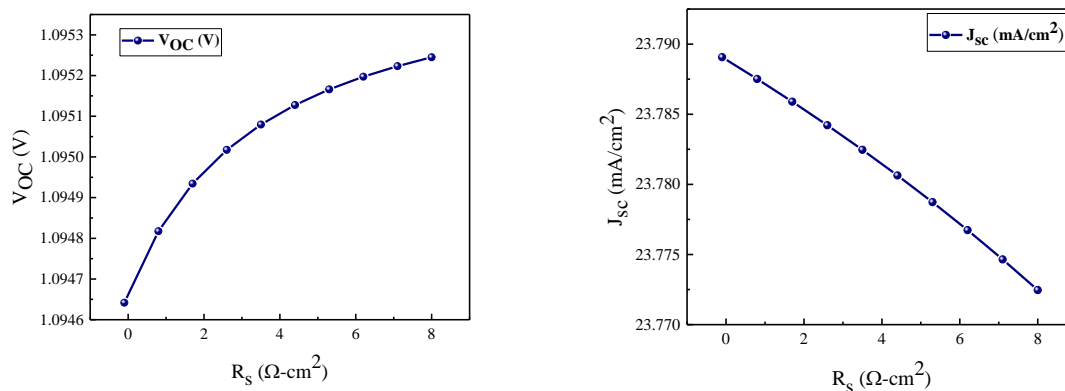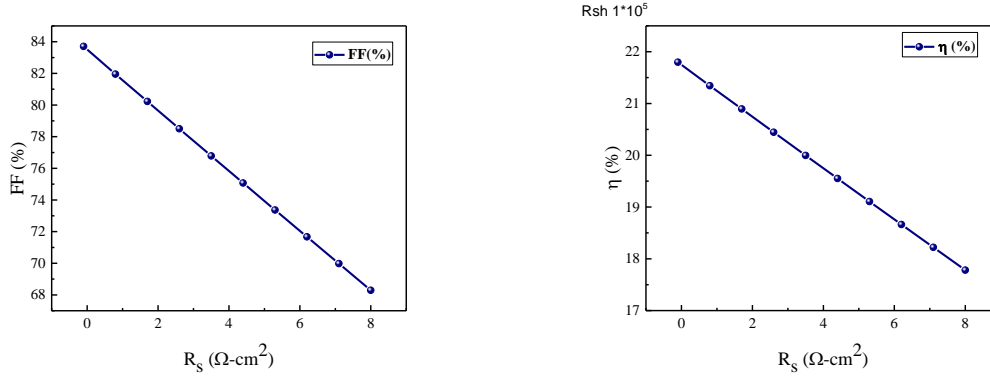
Figure 34 : Effect of the variation of PV parameters as a function of series resistance for the ETL

Shunt Resistance

The shunt (R_{Sh}) of the devices, which accounts for the leakage of current at the donor−acceptor and active layer-electrode borders, is an additional internal electrical characteristic that affects the performance of solar cells. In a forward bias connection, the greater recombination rate equates to a higher R_{Sh} value. The value of R_{Sh} is often connected to the charge recombination process (whether it be geminate or nongeminate). In other words, a reduced carrier recombination rate under light illumination, i.e., without biasing, shows that the device has a high R_{Sh} value. The J−V characteristic of a solar cell behaves normally under ideal one-sun illumination conditions, according to the Shockley equations, which can be written as eqs (20)and (21)[50]

$$J_{SC} = J_{PH} - J_0 \left[\exp\left(\frac{q(V - JR_s)}{nkT}\right) - 1 \right] - \frac{V - JR_s}{R_{sh}} \tag{20}$$

$$V_{OC} = \left(\frac{nkT}{q}\right) \ln \left\{ \frac{J_{PH}}{J_0} \left(1 - \frac{V_{OC}}{J_{PH}R_{sh}}\right) \right\} \tag{21}$$

Where J_{PH} is the photocurrent density. The effects of the variation of R_{Sh} are depicted in Figure 35. R_{Sh} is varied from 10^1 to 10^7 Ω cm^2 keeping R_s constant for of the optimized solar cell structures to observe its effect on V_{OC}, J_{SC}, FF, and PCE. It can be observed that for R_{Sh} values greater than 100 Ω, V_{OC}, J_{SC}, FF, and PCE attain constant values after increasing linearly from very low values. A detailed examination of the figure revealed that compared to J_{SC}, the increment rates for both V_{OC} and FF were greater. To be connected with the V_{OC} and FF responses, the change in R_{Sh} caused by charge transfer, the emission process, and their recombination behaviour may be more remarkable.
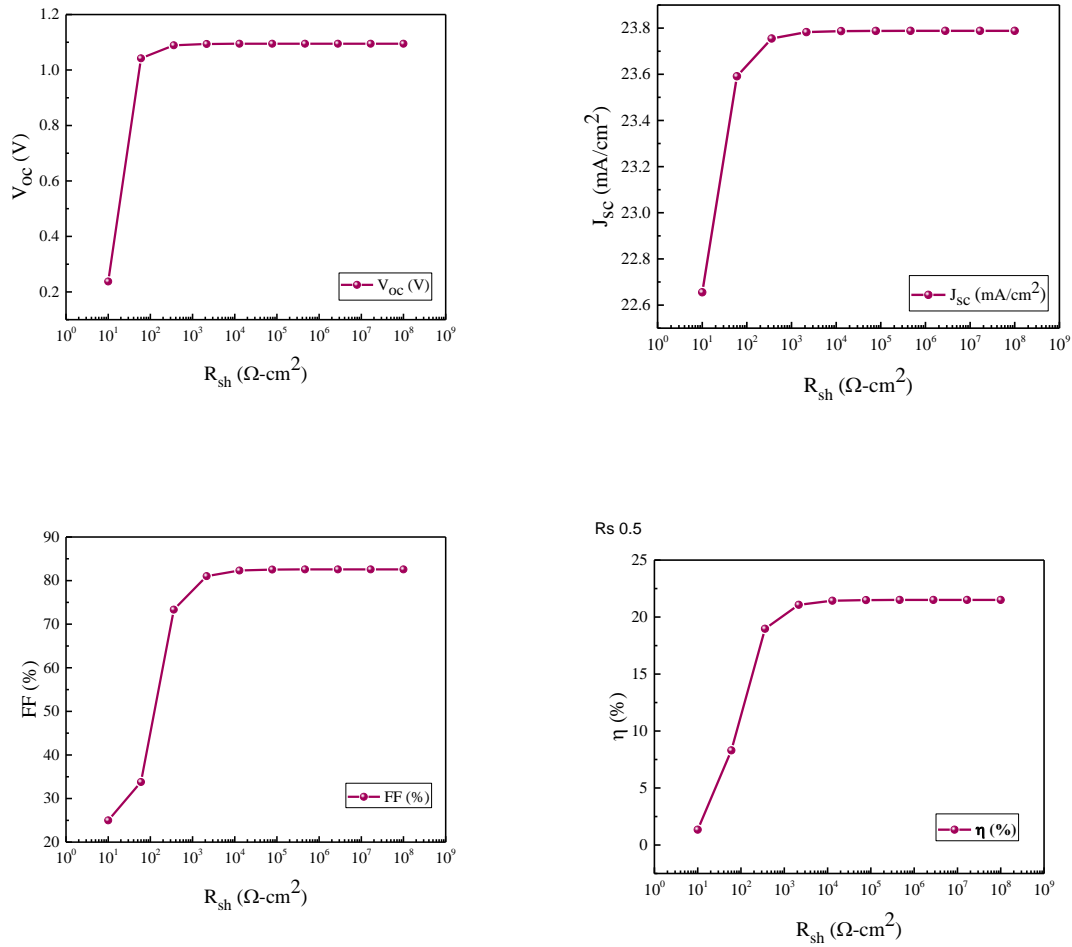
Figure 35 : Effect of the variation of PV parameters as a function of shunt resistance for the ETL

Temperature

The majority of solar cell performance demonstrates instability due to deformation between layers occurring at high temperatures. To study the relationship between temperature and solar cell efficiency, the temperature range of the simulation models was changed from 250 to 500 K. In Figure 36, the performance of the optimized solar cell structures is observed. It can be seen that the PCE, FF, and V_{OC} values decrease with increasing temperature, although the J_{SC} values remain constant. V_{OC} values decrease at high temperatures due to the increase in the reverse saturation current density (J_0) at higher temperatures, as is evident from the inverse relationship between V_{OC} and J_0 explained using eq (22)

$$V_{OC} = \frac{nkT}{q}[\ln\left(1 + \frac{J_{sc}}{J_0}\right)] \tag{22}$$

51

where denotes the thermal voltage. Furthermore, the flaws worsen when the temperature rises and V_{OC} gets smaller. So, there is a serious degradation in the SC performance as temperature increases.
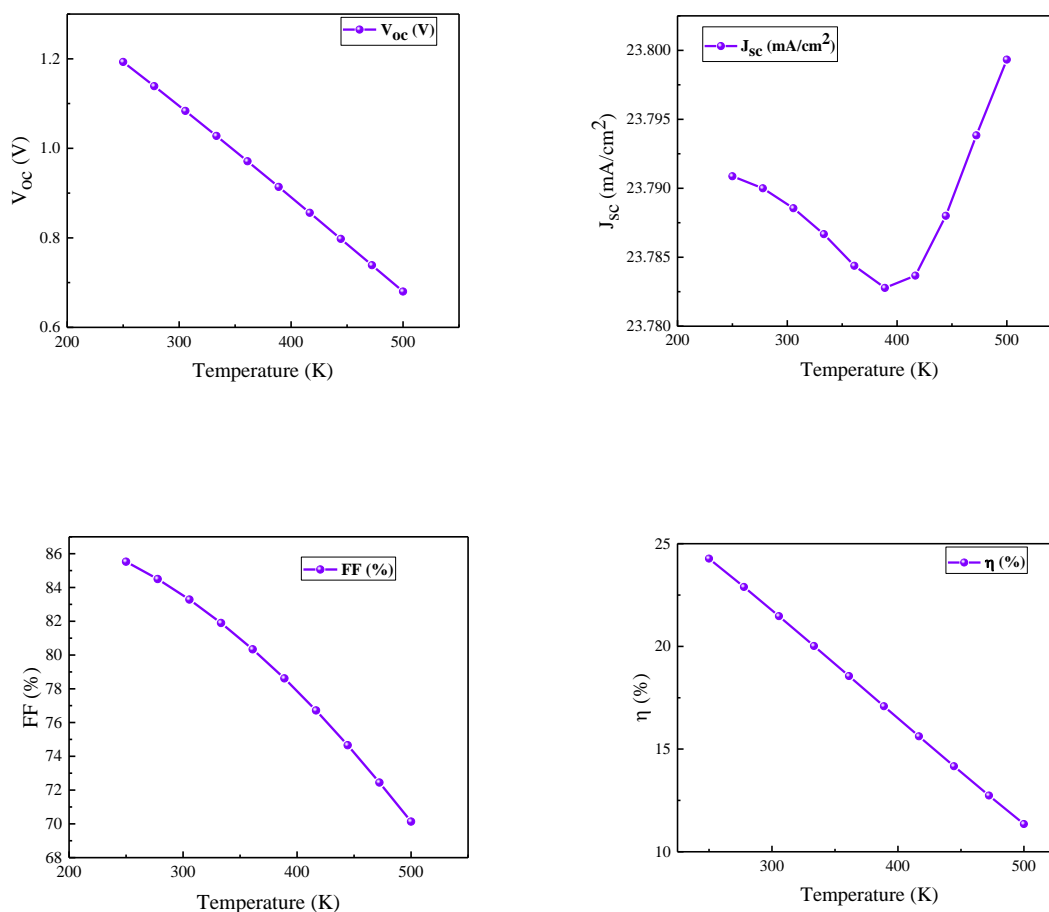

Figure 36 : Effect of the variation of PV parameters as a function of temperature for the ETL.

Effect of Capacitance and Mott−Schottky.

Mott− Schottky (M−S) is a well-known and reliable tool used to evaluate the built-in potential (Vbi), which shows the distinction between an electrode's operational functions and its amount of doping. M−S theory is mainly focused on the properties of p−n junctions, but it is also applicable to organic devices.[51] In the M−S plot, the Vbi of organic semiconductor devices is commonly represented by the x-axis intercept, and the concentration of occupied trapping centers is indicated by the slope of $1/C^2$ (V). Here, in this study, the variation of

capacitance and M−S with respect to the applied voltage is conducted in the case of optimized solar cell structures, where CBTS is taken as the HTL and TiO2 are the ETL and Cs_2BiAgI_6 is the absorber. According to Figure 16a, the capacitance increases nonlinearly with the applied voltage. M− S decreases with the voltage, which can be observed in Figure 37.
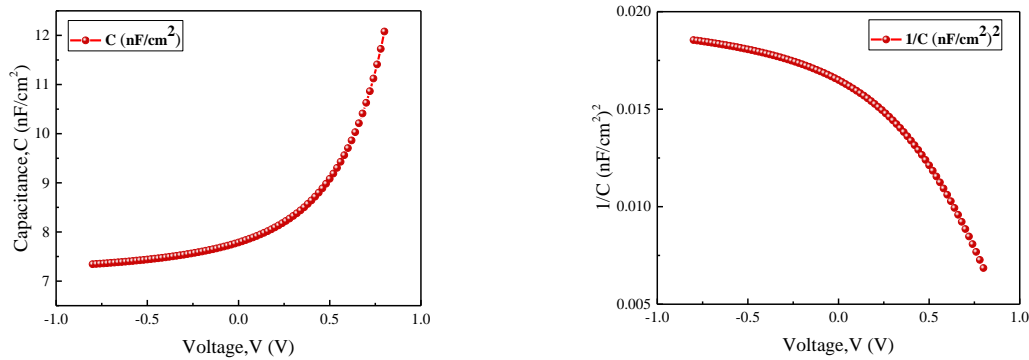

Figure 37 : Variation of Mott−Schottky (1/C2) plot, with the applied voltage for the studied PSC

Effect of Generation and Recombination Rate.

It is possible to determine the generated electron−hole pair at any point within the solar cell, for any light wavelength, or the complete standard solar spectrum. The surface of the SC structure, where the bulk of the light is absorbed, shows the highest generation rate. The generation rate of an SC is a function of both the position and wavelength and indicates how many electron−hole pairs are produced at each location of the device due to photon absorption at a particular wavelength. The generation rate is crucial for achieving the best efficiency out of SCs. PS shows the generation rate of optimized solar devices. Recombination is the opposite of generation, which involves coupling and annihilating the conduction band electrons and holes. The recombination rate is affected by the density of charge carriers and lifetime. Additionally, each defect state in the different PSC layers has an impact on the electron−hole recombination. The maximum recombination rate was observed in the range of 0.7−1.0 μm for the best solar cells as similar to the generation rate (Figure 38) position from 0.7 to 1.0 μm showed a higher recombination rate because more conduction band electrons crossed the energy barrier and entered the valence band to become more stabilized and take up the position of the valence band hole. The resulting energy levels affect the recombination rate of the

53

electron−hole within the solar device, and imperfection and grain boundaries allow the recombination rate distribution in the solar structure to be no uniform.
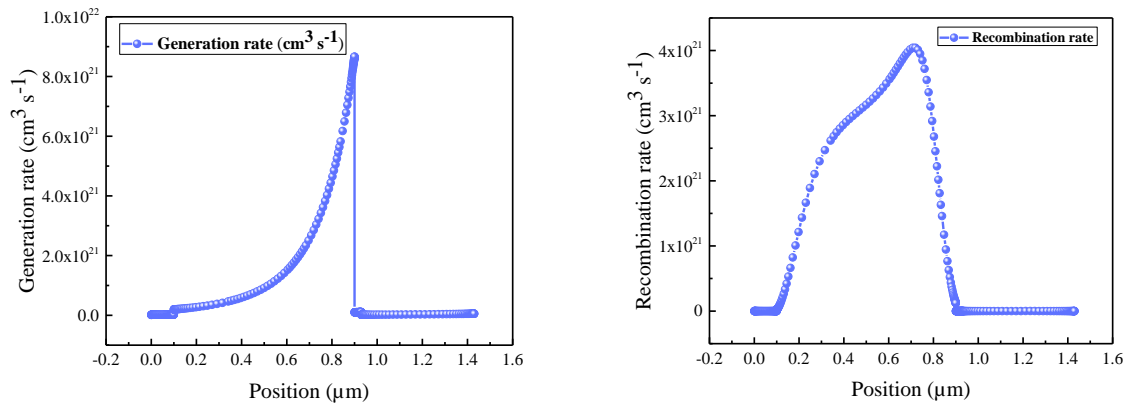

Figure 38 : Variation of capacitance (C) plot, with the applied voltage for the studied PSC

J−V and QE Characteristics.

Figure 39 shows the final optimization of the J−V characteristic curve of SCs under consideration. In contrast, at the final optimization, TiO2 ETL-associated structures showed optimum J−V characteristics Figure 39 represents the variation of quantum efficiency (QE) as a function of the wavelength of double PSC structures during and final optimization. The light wavelength affects the QE. It is the proportion of charge carriers generated by a solar cell to photons that strike the and J more photons can be absorbed by a thicker absorber, the QE typically improves with increasing absorber thickness.[61] It is observed QE is almost constant in the wavelength range from 350−700 nm and decreases thereafter under final optimized conditions Figure 39 .According to Figure 39, QE is almost 100% for TiO2 at a ∼350 nm wavelength under initial optimization conditions,
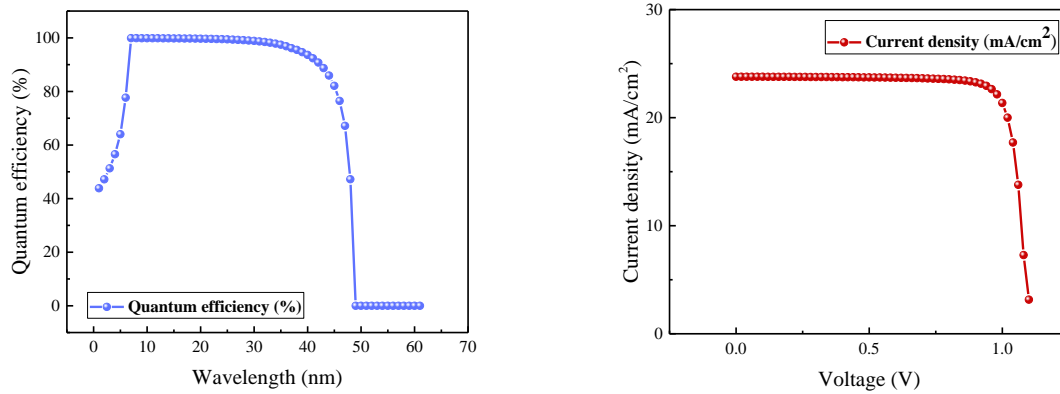
Figure 39 : Quantum efficiency curve and J-V characteristics curve

Results of SCAPS-1D Compared to Earlier Research.

The earlier study proposed optimized solar cell structures among ninety-six solar structures using SCAPS-1D software. In this study, the performance parameters of the SCs with the architectures ITO/TiO$_2$/Cs$_2$BiAgI$_6$/CBTS/Au, are optimized, and the results of the optimization study are listed in Table 7 for a fair comparison, the experimental works reported very low PCE values of less than 3% and low J$_{SC}$ in comparison to the theoretical reports. Additionally, V$_{OC}$, J$_{SC}$, and FF values of the presented work are also higher than the previously published works on the Cs$_2$BiAgI$_6$ absorber-based SC structure.

Conclusions

We used SCAPS-1D simulations to comprehensively optimize the photovoltaic characteristics of lead-free double Cs_2BiAgI_6 perovskite solar cells, and the key findings are outlined below:

The simultaneous variation of the absorber layer thickness with the acceptor density revealed that the best PCEs can be achieved with the ETLs for absorber thickness in the range of 0.5 to 1.2 μm and the N_A in the range of 1×10^9 to $7 \times 10^{17}\,cm^{-3}$. The organic ETL (PCBM) showed that the lower PCE. For the absorber layer thickness >0.5 μm and absorber defect density less than $5 \times 10^{17}\,cm^{-3}$, oxide-based ETL TiO2 exhibit the highest PCE of around 23.7%.

The PV characteristics are greatly impacted by the absorber layer and ETL thicknesses, but the HTL thickness has a negligible effect.

Although the dopant density of the absorber layer, ETL, and HTL significantly affects the PV performance of the analysed devices, the defect density of the charge transport layers has a negligible effect on the PV parameters. The amount of dopant density present in the charge transport layers influences the SC performance.

The PV parameters get much worse when the number of defects at the HTL/Cs2BiAgI6 and ETL/Cs2BiAgI6 interfaces goes up. The optimum value of the defect density for both of these interfaces was found to be $10^{10}\,cm^{-3}$ for the best SC performance.

The optimized ITO/TiO2/Cs2BiAgI6/CBTS/Au device structure delivers the best PCE of 23.71%, which is almost 20.9% higher than the experimentally fabricated Cs2BiAgI6 PSC and 8.5% higher than the theoretical device...

Table 7. Optimization Parameters, Namely, Thickness, Shallow Uniform Acceptor Density, N_A (1/cm^3), Shallow Uniform Donor Density, ND (1/cm^3), and Defect Density, Nt (1/cm3) of the HTL (CBTS), the Absorber Layer Cs_2BiAgI_6, and ETL (TiO$_2$) set layers thickness (nm) shallow uniform acceptor density, NA (1/cm^3) shallow uniform donor density, ND (1/cm3) defect density, Nt (1/cm3)

Layers	Thickness	Shallow Uniform Acceptor Density, N_A (1/cm3)	Shallow Uniform Donor Density, N_D (1/cm3)	Defect Density, N_t (1/cm3)
TiO$_2$	30	-	9×1017	1×1015
CBTS	100	1×1018	-	1×1015
Cs_2BiAgI_6	1000	1×1015	-	1×1012

Acknowledgments

References

[1]   S. Shafiee and E. Topal, "When will fossil fuel reserves be diminished?," *Energy Policy*, vol. 37, no. 1, pp. 181–189, 2009.

[2]   M. M. Halmann and M. Steinberg, *Greenhouse gas carbon dioxide mitigation: science and technology*. CRC press, 1998.

[3]   J. Asafu-Adjaye, "The relationship between energy consumption, energy prices and economic growth: time series evidence from Asian developing countries," *Energy Econ.*, vol. 22, no. 6, pp. 615–625, 2000.

[4]   C. Koroneos, A. Dompros, G. Roumbas, and N. Moussiopoulos, "Advantages of the use of hydrogen fuel as compared to kerosene," *Resour. Conserv. Recycl.*, vol. 44, no. 2, pp. 99–113, 2005.

[5]   P. Schou, "Polluting non-renewable resources and growth," *Environ. Resour. Econ.*, vol. 16, pp. 211–227, 2000.

[6]   K. Alanne and A. Saari, "Distributed energy generation and sustainable development," *Renew. Sustain. energy Rev.*, vol. 10, no. 6, pp. 539–558, 2006.

[7]   A. V Herzog, T. E. Lipman, and D. M. Kammen, "Renewable energy sources," *Encycl. life Support Syst. (EOLSS). Forerunn. Vol. Overv. life Support Syst. Sustain. Dev.*, vol. 76, 2001.

[8]   N. L. Panwar, S. C. Kaushik, and S. Kothari, "Role of renewable energy sources in environmental protection: A review," *Renew. Sustain. energy Rev.*, vol. 15, no. 3, pp. 1513–1524, 2011.

[9]   N. S. Lewis, "Toward cost-effective solar energy use," *Science (80-.).*, vol. 315, no. 5813, pp. 798–801, 2007.

[10]   A. M. Bagher, M. M. A. Vahid, and M. Mohsen, "Types of solar cells and application," *Am. J. Opt. Photonics*, vol. 3, no. 5, pp. 94–113, 2015.

[11]   P. Roy, N. K. Sinha, S. Tiwari, and A. Khare, "A review on perovskite solar cells: Evolution of architecture, fabrication techniques, commercialization issues and status," *Sol. Energy*, vol. 198, pp. 665–688, 2020.

[12]   N. NREL, "Research cell record efficiency chart,(2019)."

[13] A. Miyata *et al.*, "Direct measurement of the exciton binding energy and effective masses for charge carriers in organic–inorganic tri-halide perovskites," *Nat. Phys.*, vol. 11, no. 7, pp. 582–587, 2015.

[14] D. B. Mitzi, K. Chondroudis, and C. R. Kagan, "Organic-inorganic electronics," *IBM J. Res. Dev.*, vol. 45, no. 1, pp. 29–45, 2001.

[15] A. Kojima, K. Teshima, Y. Shirai, and T. Miyasaka, "Organometal halide perovskites as visible-light sensitizers for photovoltaic cells," *J. Am. Chem. Soc.*, vol. 131, no. 17, pp. 6050–6051, 2009.

[16] J.-H. Im, C.-R. Lee, J.-W. Lee, S.-W. Park, and N.-G. Park, "6.5% efficient perovskite quantum-dot-sensitized solar cell," *Nanoscale*, vol. 3, no. 10, pp. 4088–4093, 2011.

[17] H. S. Kim *et al.*, "Lead iodide perovskite sensitized all-solid-state submicron thin film mesoscopic solar cell with efficiency exceeding 9%," *Sci. Rep.*, vol. 2, no. 1, p. 591, 2012, doi: 10.1038/srep00591.

[18] J. Burschka *et al.*, "Sequential deposition as a route to high-performance perovskite-sensitized solar cells," *Nature*, vol. 499, no. 7458, pp. 316–319, 2013.

[19] I. Hwang, I. Jeong, J. Lee, M. J. Ko, and K. Yong, "Enhancing stability of perovskite solar cells to moisture by the facile hydrophobic passivation," *ACS Appl. Mater. Interfaces*, vol. 7, no. 31, pp. 17330–17336, 2015.

[20] F. Giordano *et al.*, "Enhanced electronic properties in mesoporous TiO2 via lithium doping for high-efficiency perovskite solar cells," *Nat. Commun.*, vol. 7, no. 1, p. 10379, 2016.

[21] W. S. Yang *et al.*, "High-performance photovoltaic perovskite layers fabricated through intramolecular exchange," *Science (80-.).*, vol. 348, no. 6240, pp. 1234–1237, 2015.

[22] X. Li *et al.*, "A vacuum flash–assisted solution process for high-efficiency large-area perovskite solar cells," *Science (80-.).*, vol. 353, no. 6294, pp. 58–62, 2016.

[23] D. Bi *et al.*, "Polymer-templated nucleation and crystal growth of perovskite films for solar cells with efficiency greater than 21%," *Nat. Energy*, vol. 1, no. 10, pp. 1–5, 2016.

[24] W. S. Yang *et al.*, "Iodide management in formamidinium-lead-halide–based perovskite layers for efficient solar cells," *Science (80-.).*, vol. 356, no. 6345, pp. 1376–1379, 2017.

[25] H.-S. Kim, A. Hagfeldt, and N.-G. Park, "Morphological and compositional progress in halide perovskite solar cells," *Chem. Commun.*, vol. 55, no. 9, pp. 1192–1200, 2019.

[26] E. A. Alharbi *et al.*, "Atomic-level passivation mechanism of ammonium salts enabling highly efficient perovskite solar cells," *Nat. Commun.*, vol. 10, no. 1, p. 3008, 2019.

[27] G. E. Eperon, S. D. Stranks, C. Menelaou, M. B. Johnston, L. M. Herz, and H. J. Snaith, "Formamidinium lead trihalide: a broadly tunable perovskite for efficient planar heterojunction solar cells," *Energy Environ. Sci.*, vol. 7, no. 3, pp. 982–988, 2014.

[28] G. Grancini *et al.*, "One-Year stable perovskite solar cells by 2D/3D interface engineering," *Nat. Commun.*, vol. 8, no. 1, p. 15684, 2017.

[29] H.-S. Kim, S. H. Im, and N.-G. Park, "Organolead halide perovskite: new horizons in solar cell research," *J. Phys. Chem. C*, vol. 118, no. 11, pp. 5615–5625, 2014.

[30] N. Sarukura *et al.*, "Proposed design principle of fluoride-based materials for deep ultraviolet light emitting devices," *Opt. Mater. (Amst).*, vol. 30, no. 1, pp. 15–17, 2007.

[31] C. Li, X. Lu, W. Ding, L. Feng, Y. Gao, and Z. Guo, "Formability of abx3 (x= f, cl, br, i) halide perovskites," *Acta Crystallogr. Sect. B Struct. Sci.*, vol. 64, no. 6, pp. 702–707, 2008.

[32] W. Travis, E. N. K. Glover, H. Bronstein, D. O. Scanlon, and R. G. Palgrave, "On the application of the tolerance factor to inorganic and hybrid halide perovskites: a revised system," *Chem. Sci.*, vol. 7, no. 7, pp. 4548–4556, 2016.

[33] M. Henini, "Principles of Electronic Materials and Devices -SO Kasap: McGraw-Hill, 2002. 745 pp, ISBN 0-07-112237-0," *Microelectronics J.*, vol. 33, no. 8, p. 681, 2002.

[34] T. Minemoto and M. Murata, "Impact of work function of back contact of perovskite solar cells without hole transport material analyzed by device simulation," *Curr. Appl. Phys.*, vol. 14, no. 11, pp. 1428–1433, 2014.

[35] M. K. Hossain, M. H. K. Rubel, G. F. I. Toki, I. Alam, M. F. Rahman, and H. Bencherif, "Effect of various electron and hole transport layers on the performance of CsPbI3-based perovskite solar cells: A numerical investigation in DFT, SCAPS-1D, and wxAMPS frameworks," *ACS omega*, vol. 7, no. 47, pp. 43210–43230, 2022.

[36] S. Srivastava, A. K. Singh, P. Kumar, and B. Pradhan, "Comparative performance

analysis of lead-free perovskites solar cells by numerical simulation," *J. Appl. Phys.*, vol. 131, no. 17, p. 175001, 2022.

[37] B. Mahapatra, R. V. Krishna, and P. K. Patel, "Design and optimization of CuSCN/CH3NH3PbI3/TiO2 perovskite solar cell for efficient performance," *Opt. Commun.*, vol. 504, p. 127496, 2022.

[38] A. Kumar, S. Maurya, S. Patwardhan, and K. R. Balasubramaniam, "Opto-electronic properties of poly-crystalline La doped BaSnO3 films deposited on quartz substrates," *J. Phys. D. Appl. Phys.*, vol. 54, no. 18, p. 185108, 2021.

[39] J. A. Owolabi, M. Y. Onimisi, J. A. Ukwenya, A. B. Bature, and U. R. Ushiekpan, "Investigating the effect of ZnSe (ETM) and Cu2O (HTM) on absorber layer on the performance of pervoskite solar cell using SCAPS-1D," *Am. J. Phys. Appl.*, vol. 8, no. 1, pp. 8–18, 2020.

[40] O. Ahmad, A. Rashid, M. W. Ahmed, M. F. Nasir, and I. Qasim, "Performance evaluation of Au/p-CdTe/Cs2TiI6/n-TiO2/ITO solar cell using SCAPS-1D," *Opt. Mater. (Amst).*, vol. 117, p. 111105, 2021.

[41] K. Lim, S. Ahn, H. Kim, M. Choi, D. H. Huh, and T. Lee, "Self-doped conducting polymer as a hole-extraction layer in organic–inorganic hybrid perovskite solar cells," *Adv. Mater. Interfaces*, vol. 3, no. 9, p. 1500678, 2016.

[42] S. Z. Haider, H. Anwar, and M. Wang, "Theoretical device engineering for high-performance perovskite solar cells using CuSCN as hole transport material boost the efficiency above 25%," *Phys. status solidi*, vol. 216, no. 11, p. 1900102, 2019.

[43] M. K. Hossain *et al.*, "An extensive study on multiple ETL and HTL layers to design and simulation of high-performance lead-free CsSnCl3-based perovskite solar cells," *Sci. Rep.*, vol. 13, no. 1, p. 2521, 2023.

[44] A. Mohandes, M. Moradi, and H. Nadgaran, "Numerical simulation of inorganic Cs 2 AgBiBr 6 as a lead-free perovskite using device simulation SCAPS-1D," *Opt. Quantum Electron.*, vol. 53, pp. 1–22, 2021.

[45] L. Huang *et al.*, "Electron transport layer-free planar perovskite solar cells: further performance enhancement perspective from device simulation," *Sol. Energy Mater. Sol. Cells*, vol. 157, pp. 1038–1047, 2016.

[46]   N. Jensen, R. M. Hausner, R. B. Bergmann, J. H. Werner, and U. Rau, "Optimization and characterization of amorphous/crystalline silicon heterojunction solar cells," *Prog. Photovoltaics Res. Appl.*, vol. 10, no. 1, pp. 1–13, 2002.

[47]   J. D. Servaites, S. Yeganeh, T. J. Marks, and M. A. Ratner, "Efficiency enhancement in organic photovoltaic cells: consequences of optimizing series resistance," *Adv. Funct. Mater.*, vol. 20, no. 1, pp. 97–104, 2010.

[48]   E. E. Van Dyk and E. L. Meyer, "Analysis of the effect of parasitic resistances on the performance of photovoltaic modules," *Renew. energy*, vol. 29, no. 3, pp. 333–344, 2004.

[49]   W. Ma, J. R. Tumbleston, M. Wang, E. Gann, F. Huang, and H. Ade, "Domain purity, miscibility, and molecular orientation at donor/acceptor interfaces in high performance organic solar cells: paths to further improvement," *Adv. Energy Mater.*, vol. 3, no. 7, pp. 864–872, 2013.

[50]   Y. Li *et al.*, "Ultra-high open-circuit voltage of perovskite solar cells induced by nucleation thermodynamics on rough substrates," *Sci. Rep.*, vol. 7, no. 1, p. 46141, 2017.

[51]   G. Garcia-Belmonte, A. Munar, E. M. Barea, J. Bisquert, I. Ugarte, and R. Pacios, "Charge carrier mobility and lifetime of organic bulk heterojunctions analyzed by impedance spectroscopy," *Org. Electron.*, vol. 9, no. 5, pp. 847–851, 2008.